# Wide-Swath Ocean Altimetry Using Multi-Satellite Single-Pass Interferometry

Theodosiou, Andreas; Kleinherenbrink, Marcel; Lopez-Dekker, Paco

**DOI**
10.1109/TGRS.2023.3287675

**Publication date**
2023

**Document Version**
Accepted author manuscript

**Published in**
IEEE Transactions on Geoscience and Remote Sensing

# Wide-Swath Ocean Altimetry Using Multi-Satellite Single-Pass Interferometry

Andreas Theodosiou, Marcel Kleinherenbrink, and Paco López-Dekker, *Senior Member, IEEE*

***Abstract*—Estimating sea surface height using cross-track interferometry requires high sensitivity because the ocean surface signal is in the order of $10\,\mathrm{cm}$. Additionally, the interferometer requires a temporal delay of a few milliseconds to ensure coherency of the moving ocean surface. We show that a squinted line of sight, in combination with a Helix satellite formation allows optimizing the effective perpendicular and along-track baselines to satisfy these conditions. This paper presents a model to estimate the performance of a formation-flying cross-track interferometer with a squinted line of sight. The tenth Earth Explorer, Harmony, which features two bistatic SAR companions, and a theoretical system with one monostatic and one bistatic SAR are used as case studies. The standard deviation of the height estimate is $1\,\mathrm{cm}$ to $10\,\mathrm{cm}$ between $29^\circ$ to $41^\circ$ and increases to $30\,\mathrm{cm}$ at the far range ($46^\circ$) at a wind speed of $5\,\mathrm{m\,s^{-1}}$. The power spectral density of the elevation shows that spatial scales of $47\,\mathrm{km}$ can be resolved. The performance improves at higher wind speeds due to higher backscattering. At a wind speed of $15\,\mathrm{m\,s^{-1}}$, wavelengths of $27\,\mathrm{km}$ to $11\,\mathrm{km}$ can be resolved, depending on the elevation spectrum. The performance over a $250\,\mathrm{km}$ swath enables the instantaneous estimation of the surface elevation at the submesoscales for the first time.**

***Index Terms*—Bistatic SAR, cross-track interferometry (XTI), ocean relative elevation measurement, formation flying, interferometry, microwave remote sensing, multistatic SAR, synthetic aperture radar.**

## I. Introduction

SATELLITE remote sensing instruments have significantly contributed to our understanding of ocean dynamics. Estimates of the sea surface height (SSH) made by radar altimeters have advanced oceanographic knowledge. Despite the plethora of SSH data that has been made available in the past decades by remote sensing instruments, ocean processes that occur at scales of $10\,\mathrm{km}$ to $100\,\mathrm{km}$, the so called *submesoscales*, are not captured in the present data. Submesoscale ocean motion plays an important role in the vertical transport of heat and nutrients [1] and the observational gap of capturing these scales has been identified [2].

Cross-track interferometry (XTI) is a technique that combines two complex-valued SAR images of the same surface, taken from different sensor positions, to estimate the relative surface height. Typical SAR instruments have swath widths in the range of $30\,\mathrm{km}$ to $250\,\mathrm{km}$ with geometric resolutions of meters up to tens of meters. Thus, an interferometric height estimate, computed at sufficiently high resolution (depending on the amount of averaging), could provide relative SSH estimates with sufficient sampling to resolve submesoscale ($10\,\mathrm{km}$ to $100\,\mathrm{km}$) phenomena such as eddies, currents, tides, and wakes from tropical cyclones.

Two properties of a cross-track interferometer that determine its performance are the perpendicular and along-track baselines. Firstly the perpendicular baseline, defined as the distance perpendicular to the line of sight (LoS) between the two sensor positions, is directly proportional to the height sensitivity. However, the maximum useful perpendicular baseline is constrained by decorrelation and the height of ambiguity. Secondly, the along-track baseline is the distance corresponding to the temporal lag between acquisitions of a given resolution cell on the imaged surface. If the surface changes during the temporal lag, the signals of the two acquisitions become decorrelated. The decorrelation manifests as noise in the interferogram and its degree depends on the rate of change of the surface. Therefore, topographic mapping of dynamic surfaces, such as the ocean, requires minimizing the along-track baseline while keeping a sufficient perpendicular baseline for sensitivity.

The requirement of a minimum along-track baseline precludes repeat-pass interferometry as a possible technique of estimating SSH. Single-pass interferometry can satisfy the requirement in the form of a single-platform interferometer or a formation-flying system of two SAR satellites. Single-platform cross-track interferometers, such as the Wide-swath Ocean Altimetry (WSOA) concept [3], overcome the issue by mechanically fixing the two SAR antennas on the satellite to physically eliminate their along-track separation. Thus, due to structural and manufacturing limitations, the two SAR antennas cannot be further apart than several meters. This limit on the cross-track separation between the antennas puts, for a given power budget, an upper bound on the sensitivity. Therefore, single-platform interferometers trade geometric sensitivity for temporal coherence.

A formation-flying interferometer achieves, given appropriate formation parameters, larger interferometric baselines between the sensors. Specifically, the Helix formation [4] allows optimizing the along-track and perpendicular separation of the satellites as a function of latitude. The formation can be configured so that the radial separation results in an along-track separation that tends to a minimum at polar latitudes and a maximum at mid-latitudes. Nevertheless, safe proximity operation constrains the minimum along-track separation above $100\,\mathrm{m}$. For an interferometer with lines of sight perpendicular to the along-track direction, which causes the along-track baseline to equal the along-track separation, this is too large for coherent acquisitions of the ocean surface.

In this paper we propose an alternative: Introducing a

A. Theodosiou, M. Kleinherenbrink and P. López-Dekker are with the Department of Geoscience and Remote Sensing, Delft University of Technology, 2628 Delft, The Netherlands.

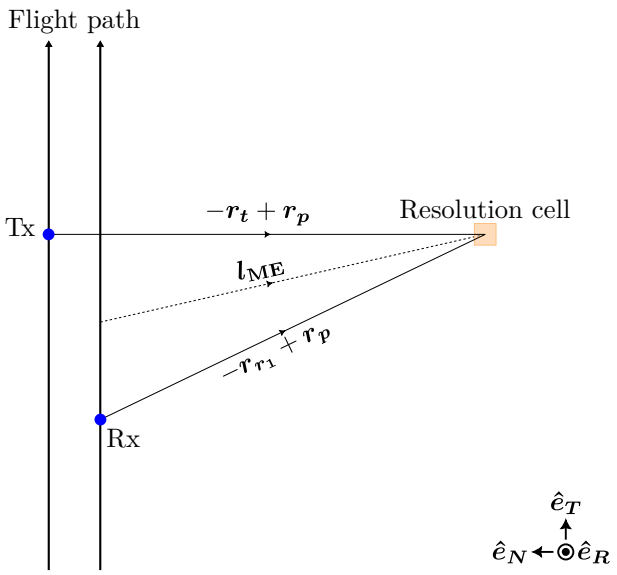


Fig. 1. Top view of the line of sight of the monostatic equivalent. $\boldsymbol{r_t}$, $\boldsymbol{r_{r_1}}$, and $\boldsymbol{r_p}$ represent the position vectors of the transmitter, the first receiver, and the resolution cell on the surface. The line of sight of the monostatic equivalent is parallel to the angle bisector, $\boldsymbol{l_{ME}}$, of the transmitter and receiver lines of sight.

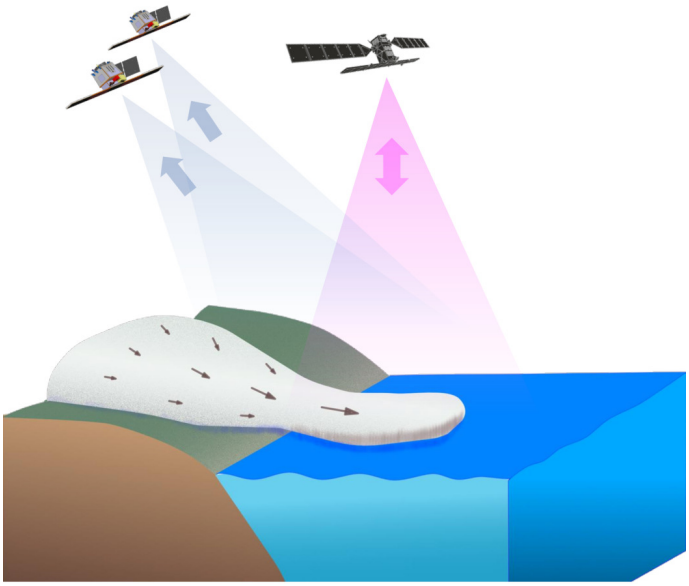

Fig. 2. The Harmony XTI configuration. The two companions, Concordia and Discordia, fly in close formation behind Sentinel-1D.

squinted line of sight to decrease the effective along-track baseline of a helix interferometer to allow estimation of relative sea-surface heights while keeping a safe radial separation. Optimizing the formation parameters allows for acquisitions with perpendicular baselines of hundreds of meters and effective along-track baselines of meters. Therefore, sensitivity is maintained while temporal decorrelation is minimized. The result is estimates of SSH with an accuracy in the order of $10\,\mathrm{cm}$ over wide swaths, enabling the recovery of mesoscale and submesoscale processes of the ocean surface in a single pass.

This paper is structured as follows: Section II explains the measurement concept, the bistatic geometry and formation, and the performance model. In Section III we discuss the performance of two interferometers: Harmony, the tenth Earth Explorer [5], and a hypothetical quasi-monostatic system of two SARs without a separate illuminator. Section IV identifies the main sources of systematic errors and outlines an estimate of their impact. Finally, Section V introduces the oceanic and atmospheric biases, with a mathematical derivation of the sea-state bias in the appendix, and their effect on the relative height estimate.

## II. Measurement Concept and Related Work

### A. Interferometric SAR Geometry

The purpose of this paper is to present a performance model for single-pass cross-track SAR interferometry over the oceans. One of the key findings that will be discussed in the subsequent sections is that a squinted line of sight, in contrast to the conventional zero-Doppler line of sight, combined with a Helix formation enables coherent acquisitions of the ocean surface. In the performance analysis, we model the formation geometry using two monostatic equivalent SARs with squinted lines of sight. The equivalent systems can represent monostatic sensors or a bistatic system. The definition of the monostatic equivalent, the relative motion of two spacecrafts in close formation, and the effective along-track and perpendicular baselines, quantities that are relevant to the interferometric performance, are discussed in the following subsections.

*1) Bistatic SAR and Monostatic Equivalent:* The geometry of a bistatic system forms an important link with the performance through the interferometric baselines. The different transmitter-to-target and target-to-receiver paths of a bistatic SAR complicate the calculation of the interferometric baseline, particularly in the case of two receivers where there is a pair of surface-to-receiver paths. The complication due to the asymmetry of the bistatic range is well known in SAR processing, where an analytic formulation of the 2-D point target spectrum does not exist for this reason. A workaround is to locate the position where a monostatic radar would measure approximately the same signal as the bistatic system. This concept is known as the monostatic equivalent in the literature [6], and it has been used to process bistatic SAR data with monostatic focusing algorithms.

Geometrically, an equivalent system reduces an illuminator and receiver pair to a single monostatic SAR. In the case of two bistatic receivers, the illuminator and the two companions are transformed to two equivalent monostatic SARs. The interferometric baseline becomes the distance between the points where the two monostatic equivalents observe a given point on the ground with the same geometry.

The monostatic equivalent of each bistatic system lies along the bisector of the bistatic angle formed by the illuminator-to-surface and the surface-to-receiver range and has a line of sight

parallel to:

$$\boldsymbol{l}_{\mathbf{ME}} = \frac{-\boldsymbol{r_t} + \boldsymbol{r_p}}{\left\|-\boldsymbol{r_t} + \boldsymbol{r_p}\right\|} + \frac{-\boldsymbol{r}_{\boldsymbol{r}_i} + \boldsymbol{r_p}}{\left\|-\boldsymbol{r}_{\boldsymbol{r}_i} + \boldsymbol{r_p}\right\|}, \tag{1}$$

where $\boldsymbol{r_t}$ is the position vector of the transmitter, $\boldsymbol{r_p}$ the position vector of the point scatterer on the surface being illuminated, and $\boldsymbol{r}_{\boldsymbol{r}_i}$ the position vector of the ith receiver where $i \in \{1, 2\}$. Figure 1 shows a visual representation of (1).

*2) Relative Motion:* Flying the SAR satellites in a Helix formation allows optimizing the along and cross-track separation for cross-track interferometry. The formation-flying elements discussed in this section apply equally to a monostatic and a bistatic SAR. In the case of Harmony, the mission consists of two passive companion satellites, which we refer to as Concordia and Discordia, flying in close formation with Sentinel-1 (S1) as the illuminator. In the XTI mission phase, Concordia and Discordia will fly behind S1, in a Helix formation [7] with a configurable along and cross-track separation, as shown in Figure 2. We employ the relative inclination and eccentricity vector formulation of relative motion [4] to model the effect of the formation on interferometric performance.

The orbital frame of reference is used as the basis for all the calculations. It consists of three unit vectors moving together: $\hat{\boldsymbol{e}}_{\boldsymbol{R}}$ along the radial direction (positive away from the Earth's center), $\hat{\boldsymbol{e}}_{\boldsymbol{T}}$ in the along-track (tangential) direction of the satellite motion, and the unit vector $\hat{\boldsymbol{e}}_{\boldsymbol{N}}$ normal to the orbital plane in the direction of the positive angular momentum vector (cross track). This triad denotes a right-handed system, with two time-dependent vectors $\hat{\boldsymbol{e}}_{\boldsymbol{R}}$ and $\hat{\boldsymbol{e}}_{\boldsymbol{T}}$; $\hat{\boldsymbol{e}}_{\boldsymbol{N}}$ is time invariant under the Keplerian approximation [4].

The relative motion of the second satellite (deputy), indicated by $C$ in Figure 3, with respect to the first (main), indicated by $M$, is expressed in the orbital frame centered on the main satellite

$$\begin{aligned}\Delta\boldsymbol{r} &= \boldsymbol{r_2} - \boldsymbol{r_1} \\ &= \Delta r_R \hat{\boldsymbol{e}}_{\boldsymbol{R}} + \Delta r_T \hat{\boldsymbol{e}}_{\boldsymbol{T}} + \Delta r_N \hat{\boldsymbol{e}}_{\boldsymbol{N}},\end{aligned} \tag{2}$$

where $\boldsymbol{r_j}$ for $j = \{1, 2\}$ is the position vector of the main and deputy satellites respectively and $\Delta r_R$, $\Delta r_T$, $\Delta r_N$ are the distances between the two satellites along the directions corresponding to each unit vector.

For near-circular orbits in close formation, which is the case for the orbits discussed in this paper, we linearize the motion according to [4]. Thus, the components of the relative position vector $\Delta r$ are

$$\begin{bmatrix}\Delta r_R/a \\ \Delta r_T/a \\ \Delta r_N/a\end{bmatrix} = \begin{bmatrix}\Delta a/a & 0 & -\Delta e_X & -\Delta e_Y \\ \Delta u & -3\Delta a/\left(2a\right) & -2\Delta e_Y & +2\Delta e_X \\ 0 & 0 & -\Delta i_Y & +\Delta i_X\end{bmatrix} \times \begin{bmatrix}1 \\ u - u_0 \\ \cos u \\ \sin u\end{bmatrix}, \tag{3}$$

where $a$ is the semi-major axis of the orbit, $\Delta\boldsymbol{e}$ and $\Delta\boldsymbol{i}$ are the differences between the eccentricity and inclination vectors

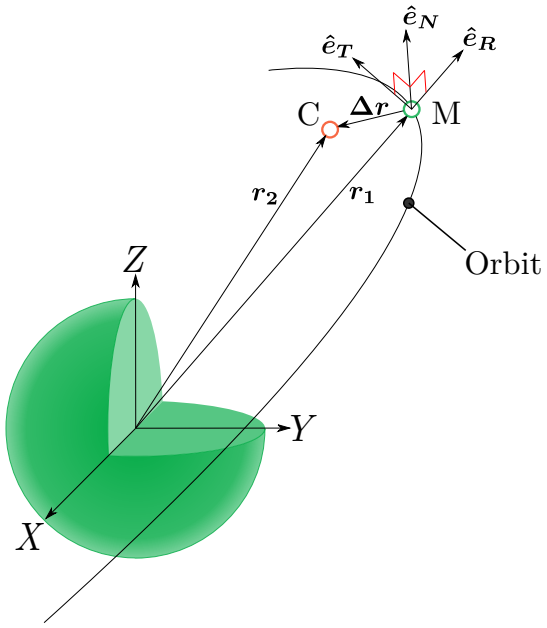


Fig. 3. Orbital frame of reference for the relative motion between two satellites.

respectively, the subscripts $X, Y$ represent the first and second components of the vector, $u$ is the mean argument of latitude, and $u - u_0$ is the argument at reference epoch $t_0$.

Setting $\Delta e_X = 0$ and $\Delta i_X = 0$ and the second component of the relative eccentricity and inclination vectors to a non-zero value provides passive stability to the formation because the two orbits are spatially separated. The two orbits pass over one another near the poles, when $u = \pi/2$, where the normal separation goes to 0 but the radial separation tends to its maximum. The opposite occurs near the equator, where the radial component goes to 0 and the normal is maximized. The oscillation of $\Delta r_R$ and $\Delta r_N$ with a phase difference of $\pi/2$ forms the known helix-like formation introduced in [4]. For the purposes of relative topography estimation, constant orbital anomaly and semi-major axis offsets are counterproductive, hence $\Delta u$ and $\Delta a$ are set to 0. Thus, the relative position vector of the formation is determined by $\Delta e_Y$ and $\Delta i_Y$. The latter is approximated by

$$\Delta i_Y \approx \Delta\Omega \sin i, \tag{4}$$

where $i$ is the inclination of the orbit and $\Delta\Omega$ is the difference in the right ascension of the ascending node of the two spacecraft.

*3) Along-Track Baseline:* A time interval between the two SAR acquisitions forming an interferogram produces a phase difference directly proportional to the velocity of the imaged surface [8]. We refer to the distance traveled in the flight direction during this time interval as the along-track (interferometric) baseline. In a conventional interferometer where both images are acquired by monostatic instruments looking along the zero-Doppler plane, the along-track baseline equals the along-track separation. For a cross-track interferometer, an along-track baseline reduces the accuracy of the height

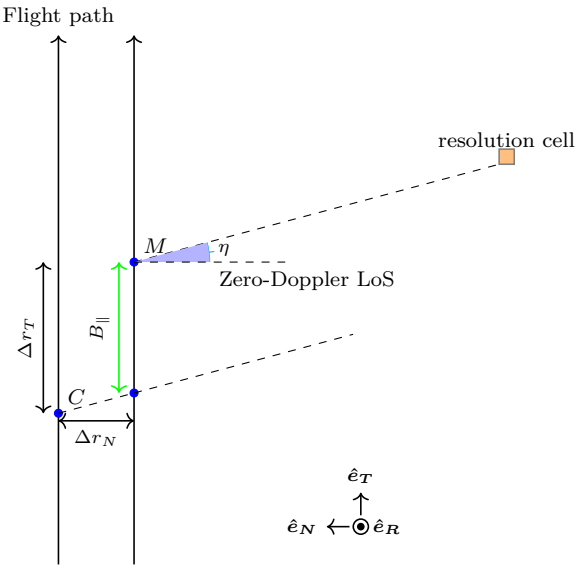


Fig. 4. Top view of the formation with a squinted line of sight. $M$ represents the position of the main and $C$ of the deputy.

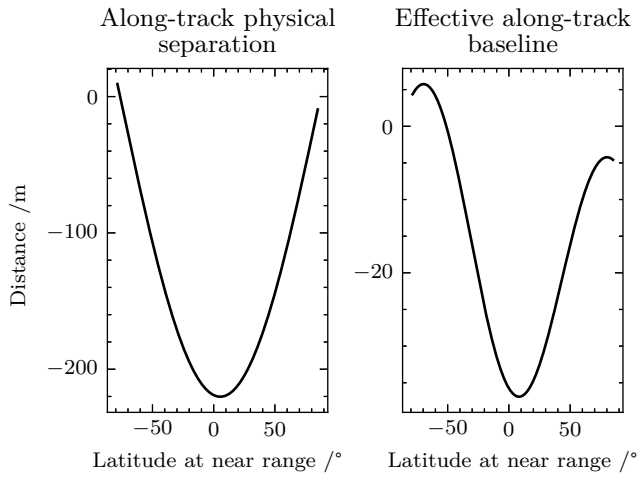


Fig. 5. The left panel shows the along-track physical separation of a formation with parameters $a\Delta e = 117\,\mathrm{m}$ and $a\Delta\Omega = 650\,\mathrm{m}$ and the right panel shows the effective along-track baseline for the same formation.

estimate because a part of the interferometric phase comes from the velocity of the surface rather than the topography.

Figure 4 illustrates the top-view geometry of two SAR satellites separated in the along and cross-track directions. The lines of sight of the two SAR antennas are looking forward with respect to the zero-Doppler direction. We give the term "squint" to the angle between the lines of sight and the zero-Doppler plane. The ground-projected squint of the antenna is labeled $\eta$. In this projection the antenna look angle is not visible as it is directed into the page.

The figure shows that for a zero Doppler configuration ($\eta = 0°$) the along-track baseline is equal to the physical separation of the two satellites in the tangential direction. If $\eta$ is non-zero, the baseline that arises due to the temporal lag is no longer the same as the physical separation. The squinted line of sight and the normal separation $\Delta r_N$ cause the second satellite to observe the same point as M, e.g. resolution cell $P$ in the diagram, before it moves $\Delta r_T$ along $\hat{\boldsymbol{e}}_T$. The effective baseline becomes

$$B_\parallel = \Delta r_T - \Delta r_N \tan\eta. \tag{5}$$

Equation (5) shows that setting $\tan\eta = \Delta r_T/\Delta r_N$ gives a zero effective along-track baseline. According to (3), the two components of interest depend on the following formation parameters $\Delta u, \Delta a, \Delta \boldsymbol{e}, \Delta \boldsymbol{i}$. For a stable formation, the dependence reduces to $\Delta e_Y$ and $\Delta\Omega \sin i$. Substituting (3) into (5) and setting the baseline to zero yields the condition that the ratio $\Delta e_Y/\Delta\Omega$ must meet:

$$\frac{\Delta e_Y}{\Delta\Omega} = \frac{\sin i}{2}\tan\eta. \tag{6}$$

Figure 5 shows the along-track physical separation and the effective along-track baseline at the near range for a set of formation parameters that have been optimized according to (6). We note that while the separation reaches $230\,\mathrm{m}$ the effective baseline has a maximum magnitude of $38\,\mathrm{m}$. The variation of the effective along-track baseline follows this sinusoidal pattern for all incidence angles with decreasing amplitude towards the middle range and increasing amplitude from the middle to the far range. The effective baseline does not exceed $80\,\mathrm{m}$ for this set of formation parameters.

*4) Perpendicular Baseline:* To discuss the calculation of the perpendicular baseline we start from a non-squinted configuration where the two SAR sensors are in the same radial-normal plane. We consider the projection along the radial-normal plane as illustrated in Figure 6. The perpendicular baseline $B_\perp$ is the distance between the two planes spanned by the flight direction (along-track) and the line of sight (antenna beam-pointing direction) of each satellite:

$$\begin{aligned} B_\perp &= b_{X_1} + b_{X_2}, \\ &= \Delta r_N \cos\theta + \Delta r_R \sin\theta. \end{aligned} \tag{7}$$

Introducing a squint to the line of sight changes the effective perpendicular baseline, as was the case for the along-track baseline. Figure 7 illustrates such a configuration. To find the effective baseline, the line of sight and the co-registration need to be taken into account. As discussed in Section II-A3, after co-registration of the two SAR images, the along-track separation of the two sensors becomes $\Delta r_N \tan\eta$. This is equivalent to rolling forwards the position of the deputy satellite along its orbital path so that it shares the same radial-line-of-sight plane as the main satellite.

At the point where the two satellites view the same resolution cell their separation is given by

$$\boldsymbol{b_{3D}} = \begin{pmatrix} \Delta r_R \\ \Delta r_N \tan\eta \\ \Delta r_N \end{pmatrix}, \tag{8}$$

where $\tan\eta$ is the tangent of the ground-projected squint. $\tan\eta$ is also given by the ratio of the along-track component

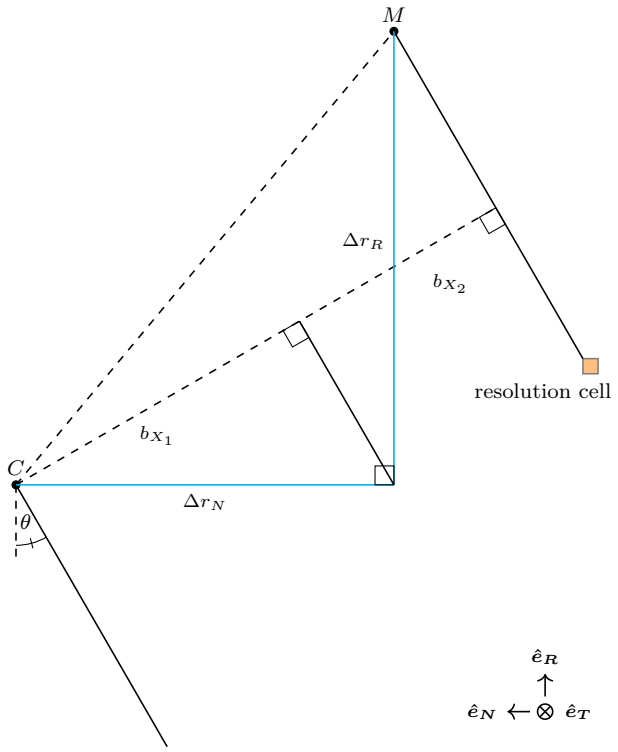


Fig. 6. View along the radial-normal plane. The squint angle in this view would be into/out of the page. The look angle $\theta$ is the angle formed by the direction of the beam center and the nadir.

to the normal component of the unit vector parallel to the line of sight $\hat{\boldsymbol{l}}$. The perpendicular baseline is given by

$$\begin{aligned} B_\perp &= \|\boldsymbol{b_{3D}}\| \sin\psi, \\ &= \left\|\boldsymbol{b_{3D}} \times \hat{\boldsymbol{l}}\right\|, \end{aligned} \tag{9}$$

where $\psi$ is the angle between $\boldsymbol{b_{3D}}$ and $\hat{\boldsymbol{l}}$. Equation (9) shows that the physical separation components and ground-projected squint can be tuned to give a $B_\perp$ that is sufficiently large to offer good sensitivity to height. At the same time, $\Delta r_T$ does not affect $B_\perp$, thus it can be selected together with angle $\eta$ to minimize $B_\parallel$ according to (5). Equation (9) shows that the effective perpendicular baseline is the projection of the physical separation perpendicular to the line of sight, after aligning the lines of sight of the two receivers. Therefore it largely follows the perpendicular baseline of the formation which varies sinusodially with the mean argument of latitude with a maximum around $0^\circ$ and minimums towards the poles where the two satellites cross each other. Due to the squint the amplitude of the sinusodial variation decreases slightly with incidence angle.

### B. Cross-track Interferometry Model

In monostatic systems, the two-way range difference between the two instruments and the surface can directly be coupled to surface elevation. For single-transmitter systems, such as a single-pass interferometer where only one SAR transmits, the same is true except that it only depends on the single-way range difference. The interferometric phase

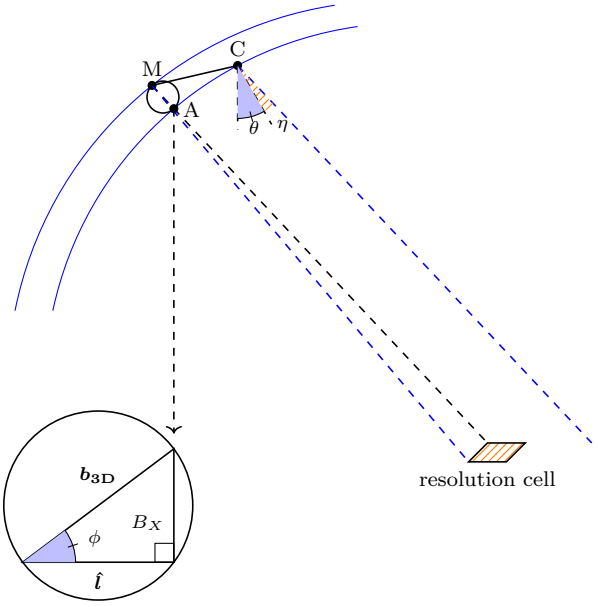


Fig. 7. Cross-track baseline with squinted line of sight.

between two images of the same scene obtained from two SARs is

$$\phi = -p\frac{2\pi}{\lambda}\Delta R_s, \tag{10}$$

where $p = 2$ for "ping-pong" systems and $p = 1$ for single-transmitter systems, $\lambda$ is the carrier wavelength and $\Delta R_s$ is the slant range difference from a point on the surface to the two antennas. The expression for the phase difference can be approximated by

$$\phi \approx -\frac{2\pi}{h_a}\Delta h, \tag{11}$$

where $\Delta h$ is the relative height of the surface and $h_a$ is the height of ambiguity:

$$h_a = \frac{\lambda R_s \sin\theta_i}{pB_\perp}, \tag{12}$$

where $R_s$ is the slant range and $\theta_i$ is the incident angle. The height of ambiguity is used in the performance model to convert the interferometric phase error to the height estimate error.

### C. Measurement Error

*1) General Model:* The interferometric phase measured by a single-pass cross-track interferometer, where the two satellites are in a close formation, will have contributions both from the topography of the scene $\phi_{\text{topo}}$ and from motion in the direction of the line of sight $\phi_\parallel$ due to the perpendicular and along-track baseline respectively. Additionally, the interferrometric phase signal $\phi$ will be modified by white noise $\phi_n$ due to the thermal noise of the SAR electronics and the decorrelation of the scene

$$\phi = \phi_{\text{topo}} + \phi_\parallel + \phi_n. \tag{13}$$

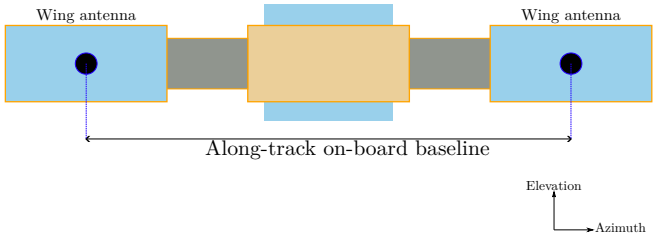


Fig. 8. The planar antenna array assumed by the performance model. Two phase centers are positioned at the aft and fore of the antenna structure.

We assume that the receiving SAR instruments follow the design of the Harmony companions. Each has a planar antenna made from two subapertures separated along the antenna longitudinal axis. One subaperture is at the aft of the antenna structure and the other at the fore as illustrated in Figure 8. Each of the two subapertures forms a separate SAR image. The instrument forms an improved SAR image by combining the images from the individual phase centers, resulting in a better Noise-equivalent Sigma Zero (NESZ) and Azimuth Ambiguity to Signal Ratio (AASR). Unless stated otherwise, the imaging and interferometric performance discussed in the paper refer to the performance of the combined signal rather than that of the single-channel signal.

Each receiving SAR estimates the phase due to the motion of the surface $\phi_{\parallel}$, also known as the "along-track interferometry (ATI) phase", using its two individual phase centers. The estimate $\hat{\phi}_{\parallel}$ is subtracted from the measured phase to remove the undesired motion component, giving an estimate of the topographic phase. The error of the height estimate includes the error of estimating the ATI phase $\epsilon_{\parallel}$

$$\hat{\phi}_{\text{topo}} = \phi_{\text{topo}} + \epsilon_{\parallel} + \phi_n, \tag{14}$$

$$\epsilon_{\parallel} = \phi_{\parallel} - \frac{B_{\parallel}}{B_{\parallel s}}\hat{\phi}_{\parallel}, \tag{15}$$

where the estimate of the ATI phase acquired using the two on-board phase centers is scaled by $B_{\parallel}/B_{\parallel s}$. The scaling factor arises because the estimate of the motion phase is obtained with the on-board along-track baseline, $B_{\parallel s}$, which is different from the effective baseline of the formation.

We use the Cramer-Rao lower bound [9] to estimate the standard deviation of the interferometric phase

$$\sigma_{\phi} = \sqrt{\frac{1-\gamma^2}{2N_l\gamma^2}}, \tag{16}$$

where $\gamma$ is the coherence and $N_l$ is the number of independent looks. The coherence is the product of the partial coherence factors [10]

$$\gamma \approx \gamma_{\text{SNR}}\gamma_B\gamma_t\gamma_{\text{Amb}}\gamma_{\text{Vol}}, \tag{17}$$

where the right-hand side of the equation describes the contributions to the error due to noise including quantization errors ($\gamma_{\text{SNR}}$), baseline decorrelation ($\gamma_B$), temporal decorrelation ($\gamma_t$), ambiguities ($\gamma_{\text{Amb}}$), and volumetric scattering ($\gamma_{\text{Vol}}$). Since the effect of ambiguities on Harmony is addressed in [11], we do not consider it in this paper.

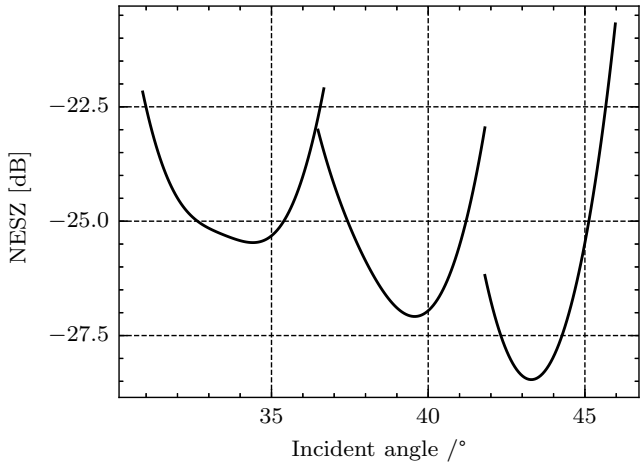


Fig. 9. The estimated NESZ of Harmony with Sentinel-1 as the illuminator. The three subswaths of Sentinel-1's IW mode are visible by the discontinuities between the three quadratic curves.

At C-band, the electromagnetic signal practically does not propagate into the water. However, scatterers within a resolution cell follow the highly varying surface topography of the ocean, which produces volumetric decorrelation. We follow the same approach as in [12] and model the mean topographic height of the ocean surface as a Gaussian variable with zero mean. The volumetric decorrelation due to the surface waves is given by

$$\gamma_{\text{Vol}} = \mathrm{e}^{-\frac{1}{2}(2\pi/h_a)^2\sigma_h^2}, \tag{18}$$

where the standard deviation of the ocean height is related to the significant wave height (SWH) by $\text{SWH} = 4\sigma_h$.

The coherence due to temporal decorrelation depends on the temporal lag between acquisitions [13]

$$\gamma_t = \mathrm{e}^{-\tau^2/\tau_c^2}, \tag{19}$$

where $\tau = \frac{B_{\parallel}}{2v}$ is the lag between acquisitions due to the effective along-track baseline $\frac{B_{\parallel}}{2}$ and platform velocity $v$, and $\tau_c \approx 3.29\lambda/U$ approximates the coherence time at wind speed $U$ [10].

Baseline decorrelation occurs due to spectral shifts between SAR acquisitions with different incidence angles. However, filtering the two SAR signals to a common frequency band avoids the decorrelation [14] at the cost of reducing the effective number of looks. We assume that the SAR signals are filtered to correct for the spectral shift. Therefore, we assume $\gamma_B = 1$ and account for the reduction in the number of looks by a factor $\gamma_B = 1 - B_{\perp}/B_{\perp,c}$, where $B_{\perp,c}$ is the critical baseline [15].

*2) Instrument Specific Parameters:* The coherence due to noise depends on the signal-to-noise ratio (SNR), which is a

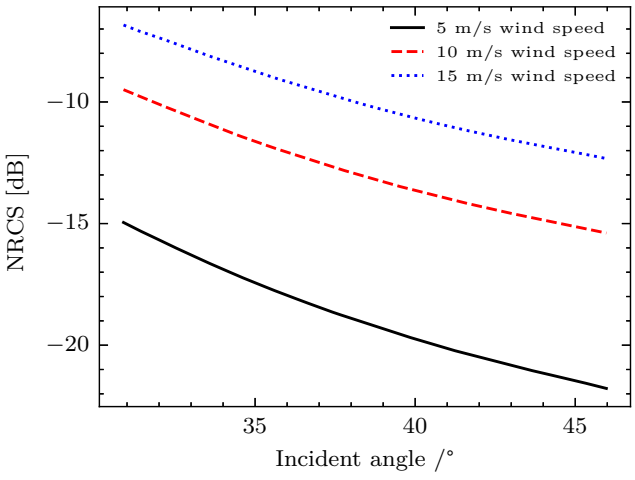


Fig. 10. The estimated NRCS in the vertical co-polarized channel for Harmony over a sea surface that is driven by a wind with speeds $5\,\mathrm{m\,s^{-1}}$, $10\,\mathrm{m\,s^{-1}}$ and $15\,\mathrm{m\,s^{-1}}$. The magnitude of the normalized radar cross-section falls as the incidence angle moves towards the far range. .

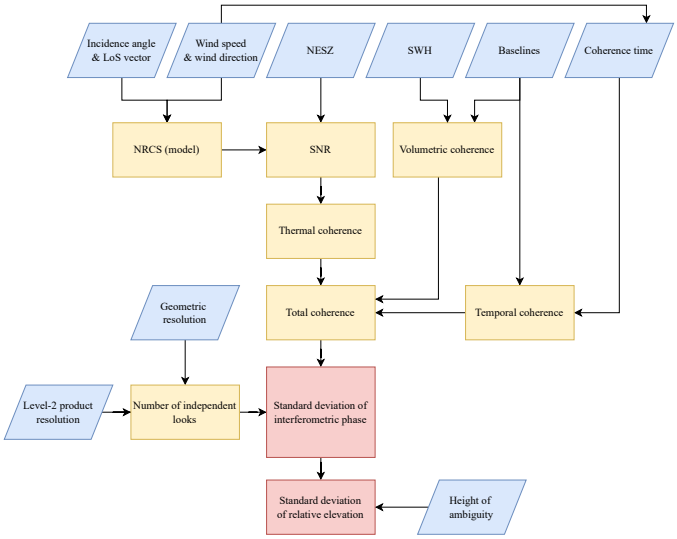


Fig. 11. Flowchart of the interferometric height standard deviation calculation.

function of the NESZ and the normalized radar cross-section (NRCS), $\sigma^0$, of a given resolution cell [16] [17]

$$\gamma_{\mathrm{SNR}} = \frac{1}{1 + \mathrm{SNR}\,(\sigma^0, \mathrm{NESZ})^{-1}}. \tag{20}$$

The NESZ depends on the system parameters and the antenna gains of both the transmitter and receiver. Thus, to produce performance estimates, assumptions need to be made about the antenna gain and pattern. In the Harmony case study the antenna pattern of the transmitter is calculated using the specification of Sentinel-1. The effective area of the Harmony companions is computed for three elements with identical, $2.6 \times 0.66\,\mathrm{m}$, fore and aft elements that are separated by $10\,\mathrm{m}$. The dimensions were selected to match the design from industry. When all phase centers on-board the Harmony satellites are used as a single antenna, the NESZ varies from $-22\,\mathrm{dB}$ to $-28.5\,\mathrm{dB}$ as shown in Figure 9. In the quasi-monostatic case study, the transmit and receive antennas are the same and any realistic parameters can be used. However, as will be explained in the next section, the aim of the quasi-monostatic case is to illustrate the effect of optimizing the squint without being constrained by the need to have a good overlap of the receiver and transmitter beams on the surface. Thus, all system parameters, including the NESZ, NRCS, and on-board phase center separation, are kept the same with those in the Harmony case with the exception of the antenna squint.

The backscattering coefficient of a SAR system observing the ocean surface depends on many factors such as: the instrument viewing geometry, surface roughness, the dielectric properties of the sea, and the waves being driven by the wind. Three mechanisms drive the wave-induced changes to the backscattered power: specular reflection, Bragg scattering, and wave breaking. We apply a multistatic NRCS model based on the model developed by Yuan [18] to the geometry of Harmony, i.e. the incident and scattered azimuth and incidence angles due to the separation of transmitter and receiver, to estimate $\sigma^0$ at different wind speeds. The NRCS for $5\,\mathrm{m\,s^{-1}}$, $10\,\mathrm{m\,s^{-1}}$ and $15\,\mathrm{m\,s^{-1}}$ downwind is shown in Figure 10.

The number of independent looks is the ratio of the product resolution $\rho_{\mathrm{L2}}$ and nominal geometric resolution $\rho_{\mathrm{2D}}$

$$N_l = \gamma_B \frac{\rho_{\mathrm{L2}}}{\rho_{\mathrm{2D}}}. \tag{21}$$

Sentinel-1 in IW mode has a spatial resolution of $5\,\mathrm{m} \times 20\,\mathrm{m}$. The level-2 product resolution depends on the accuracy we want to achieve. For relative elevation measurements with accuracy of $10\,\mathrm{cm}$ over the majority of the swath and latitudes, $3\,\mathrm{km} \times 3\,\mathrm{km}$ is sufficient which corresponds to $N_l = 90 \times 10^3$.

With the geometry of the formation, the number of looks and the SNR determined we compute the total coherence of the interferometer

$$\gamma = \gamma_{\mathrm{SNR}} \gamma_t \gamma_{\mathrm{Vol}}. \tag{22}$$

Following the same procedure, we also calculate the coherence due to the temporal and thermal decorrelation of the ATI phase estimate. Volumetric decorrelation does not impact the on-board along-track phase estimate because the separation of the phase centers only has a small residual perpendicular component. The standard deviation for these two sources of uncertainty is calculated using the Cramer-Rao lower bound given in (16). Due to the addition of the estimation error to the estimate of the topographic phase (14), the uncertainty of the ATI phase estimate contributes to the overall system uncertainty

$$\sigma_\phi = \sqrt{\sigma^2_{\phi_n} + \left(\frac{B_\parallel}{B_{\parallel s}}\right)^2 \sigma^2_{\hat{\phi}_{\mathrm{ATI}}}}. \tag{23}$$

The addition of the two uncertainties implicitly assumes that the two are statistically independent. Figure 11 shows a schematic representation of the method used to obtain the standard deviation of the height estimate. The process illustrated in

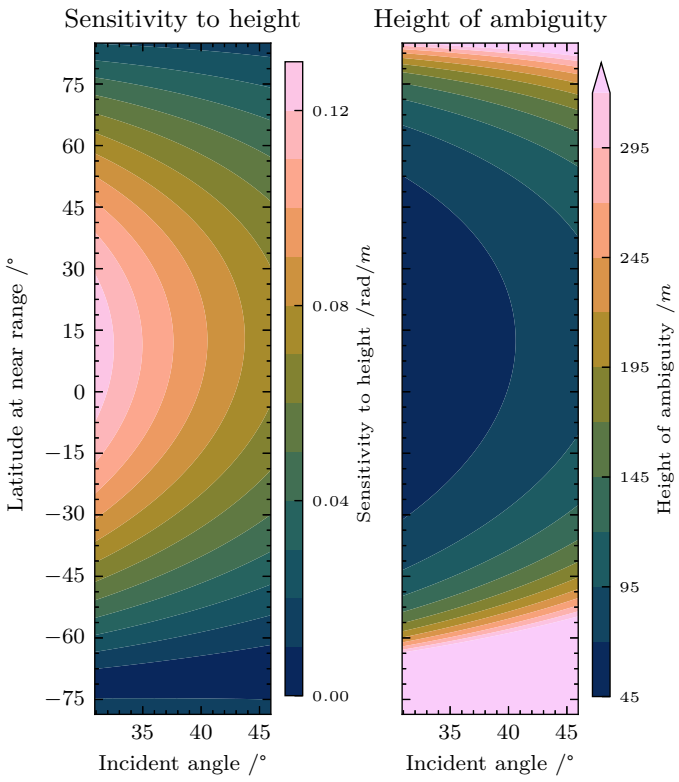


Fig. 12. Harmony's sensitivity to height and height of ambiguity of the optimized formation. The latitudes of maximum sensitivity and minimum height of ambiguity occur where the effective perpendicular baseline reaches its maximum.

the flowchart is applied separately to the main interferometer, formed by the Helix formation of SAR satellites, and to the along-track on-board interferometer, formed by the two wing phase centers on-board each satellite, to calculate $\sigma_{\phi_n}$ and $\sigma_{\hat{\phi}_{\mathrm{ATI}}}$. The SNR of the latter is less than the SNR of the former because only one of the phase centers of the receive antenna is used to obtain the on-board ATI phase estimate. Additionally, the temporal coherences of the two systems differ due to the different geometry of the satellite formation compared to the two phase centers on-board one of the two companions. The on-board ATI phase estimate has a fixed purely along-track baseline between the two phase centers while the effective baseline of the main interferometer varies along the orbit due to the Helix formation.

## III. Performance Analysis

The interferometric model presented in Section II-B is applied to two case studies: the Harmony companions with Sentinel-1 as the transmitter; A pair of SARs in a Helix formation with one of the two acting as the transmitter. We use a wind speed of $5\,\mathrm{m\,s^{-1}}$ in both case studies, while the performance of Harmony is also evaluated at $U = 10\,\mathrm{m\,s^{-1}}$ and $U = 15\,\mathrm{m\,s^{-1}}$ to assess the change in performance with wind speed. For the purposes of interferometric performance the track is symmetric over the ascending and descending parts of the orbit; Hence, only the descending part of the orbit is used to compute the results. In both case studies, once the state vector of the main satellite of the Helix formation is determined, the position of the deputy satellite is computed by applying the formation parameters to (3). Then, the relative position vector and the line of sight of the main satellite are used in (5) and (9) to calculate the effective baselines. With the effective baselines computed, the measurement uncertainty is calculated as explained in II-C.

TABLE I
Relevant orbital and processing parameters. IW refers to Sentinel-1's Interferometric Wide Swath operating mode. The number of independent looks is calculated according to (21) for a product resolution of $3\,\mathrm{km} \times 3\,\mathrm{km}$ and the nominal geometric resolution of S1 in IW mode ($5\,\mathrm{m} \times 20\,\mathrm{m}$).

| Parameter | Value | Unit |
|---|---|---|
| Centre frequency | 5.405 | GHz |
| Platform mean speed | 7590 | $\mathrm{m\,s^{-1}}$ |
| Incident angle Senintel-1 (IW) | 30–46 | ° |
| Lag between Sentinel-1 and Harmony formation | 350 | km |
| Separation due to inclination difference | 0 | m |
| Companion constant along-track separation | 0 | m |
| Number of independent looks | $90 \times 10^3$ | - |

### A. Harmony

Sentinel-1 [19] defines the reference orbit and the Harmony companions fly in a Helix formation lagging Sentinel-1 by $350\,\mathrm{km}$. The parameters relevant to the model are listed in Table I. Once the orbit of Sentinel-1 is computed, the position of the first companion, Concordia, which is used as the reference vehicle of the close formation, is calculated using the same orbital parameters as Sentinel-1 but with the mean anomaly of the orbit at the same epoch shifted to lag S1 by $350\,\mathrm{km}$. Thus, Concordia travels in the same orbital plane as S1 with a mean lag of $350\,\mathrm{km}$ and Discordia has an orbit relative to Concordia determined by the formation parameters.

SAR imaging requires sufficient overlap of the transmitter and receiver beam on the imaged surface. Hence, Concordia steers its antenna beam to align with that of Sentinel-1 on the surface, leading to a range dependent squint. As a result, $\tan\eta$ cannot freely adhere to (6) to minimize $B_\parallel$. $B_\parallel$ passes through zero if the ratio of $e_Y$ to $\Delta\Omega$ follows (6). However, the squint of the receiver decreases with range as it tracks the line of sight of the illuminator. Consequently, $B_\parallel$ cannot be reduced to 0 for the entire swath.

The close formation is defined by two parameters: the vertical separation due to a difference in the magnitude of the eccentricity vector $a\Delta e$, and a horizontal separation due to a difference in the ascending nodes $a\Delta\Omega$. Two formations are considered in the analysis: One that does not follow the condition shown in (6) for minimizing $B_\parallel$; and a second formation that does so that the effect of using the squint to enhance performance can be illustrated. The parameters of the two formations are listed in Table II.

The careful reader would raise the question of the optimal combination of $\Delta e$ and $\Delta\Omega$. Forcing the along-track baseline to go through zero can be achieved by selecting $\Delta e$ and $\Delta\Omega$ to follow the ratio of (6). However, the condition places no

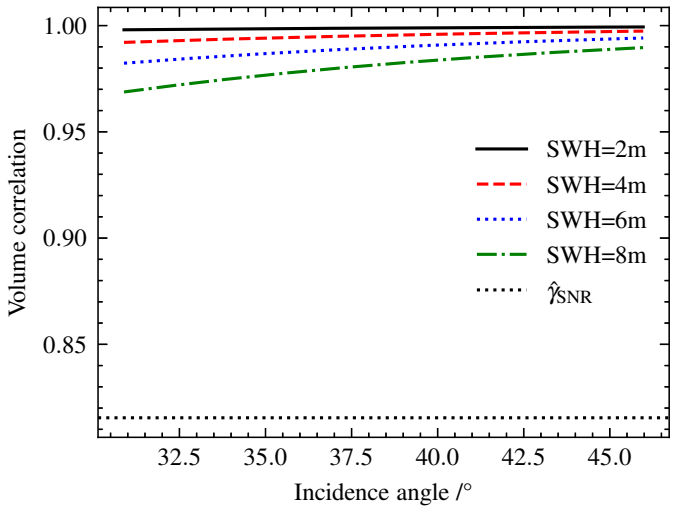


Fig. 13. The volumetric correlation as a function of incidence angle for different values of significant wave height. The mean thermal coherence is plotted using the black dashed line.

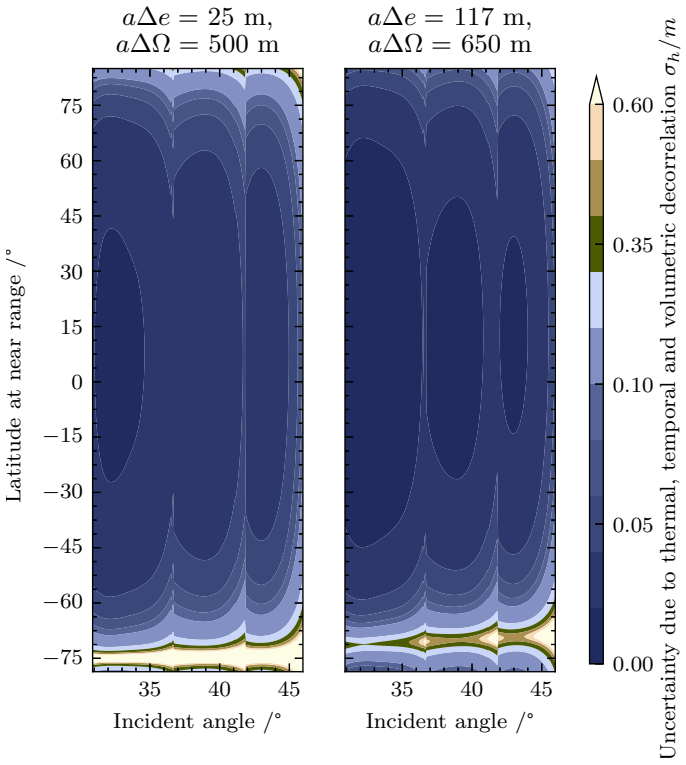


Fig. 14. The estimated SSH uncertainty of the system due to thermal, spatial and temporal decorrelation of the signal in terms of $1\sigma$ at a wind speed of $5\,\mathrm{m\,s^{-1}}$.

TABLE II
THE TWO COMPANION FORMATIONS CONSIDERED IN THE SIMULATIONS. WE REFER TO THE FIRST AS THE UNOPTIMIZED FORMATION AND TO THE SECOND AS THE OPTIMIZED FORMATION. EACH IS DEFINED BY THE VERTICAL SEPARATION DUE TO A DIFFERENCE IN THE MAGNITUDE OF THE ECCENTRICITY VECTOR $a\Delta e$, AND A HORIZONTAL SEPARATION DUE TO A DIFFERENCE IN THE ASCENDING NODES $a\Delta\Omega$.

| $a\Delta e$/m | $a\Delta\Omega$/m |
|---|---|
| 25 | 500 |
| 117 | 650 |

constraints on the magnitude of the values. A strategy of having the smallest $B_{\parallel}$ at all latitudes and incidence angles would require selecting the smallest possible values that are operationally safe. Yet, this would mean that sensitivity to height would be too small to achieve good performance. On the other hand, raising the two parameters leads to higher sensitivity at the cost of higher extreme values of along-track baseline and smaller height of ambiguity. Heights of ambiguity smaller than $30\,\mathrm{m}$ can cause phase-unwrapping problems in regions with rough terrain.

Since Harmony will also perform acquisitions over land, the formation parameters of the optimized case were selected as the highest values that provide a minimum $h_a = 30\,\mathrm{m}$. Figure 12 shows the sensitivity and height of ambiguity of Harmony for the optimized formation. The sensitivity reaches its maximum at the middle latitudes where the effective perpendicular baseline is at its largest value. The sensitivity varies from $0.01\,\mathrm{rad\,m^{-1}}$ to $0.13\,\mathrm{rad\,m^{-1}}$, with the exception of a zone from $67.5°$ to $71.25°\mathrm{S}$ where the satellites of the formation cross and the separation tends to zero causing the sensitivity to also tend to zero. The height of ambiguity follows the inverse progression ranging from a minimum of $45\,\mathrm{m}$ to a maximum of $1000\,\mathrm{m}$. Values above $300\,\mathrm{m}$ are not shown in the plot to avoid losing the detail in the variation of the small values of $h_a$ which are critical. The sensitivity and height of ambiguity of the non-optimized formation follow the same pattern as those of the optimized formation but the sensitivity has a maximum at $0.10\,\mathrm{rad\,m^{-1}}$ and the height of ambiguity a minimum of $60\,\mathrm{m}$.

An additional parameter that affects the performance is the significant wave height. The volumetric decorrelation depends inversely on the SWH and the sensitivity. Figure 13 illustrates $\gamma_{\mathrm{Vol}}$, at the latitude with the largest perpendicular baseline of the optimized formation, for different values of SWH and the mean $\gamma_{\mathrm{SNR}}$ as a function of incidence angle. The figure shows that even at $8\,\mathrm{m}$ of significant wave height, the volumetric decorrelation is not as significant as thermal decorrelation. From this point on, we assume a significant wave height of $6\,\mathrm{m}$ for both case studies, which is a conservative number since the majority of the ocean has smaller waves.

Figure 14 illustrates the estimated sea surface height error of the interferometer at a wind speed of $5\,\mathrm{m\,s^{-1}}$. The error shown in the figure is due to the thermal, temporal and volumetric decorrelation of the signal. The results show that the error is within $5\,\mathrm{cm}$ over the majority of the swath and latitudes. The performance rapidly deteriorates close to the poles because the two companions fly over one another and $B_{\perp}$ tends to its minimum value. In turn, the height of ambiguity tends to its maximum, pushing the uncertainty up. At the midpoint of an ascending or descending pass, the coherence due to the time lag $\tau$ is at its minimum because $B_{\parallel}$ reaches its maximum at the near range. However, this is not visible because $B_{\perp}$ tends

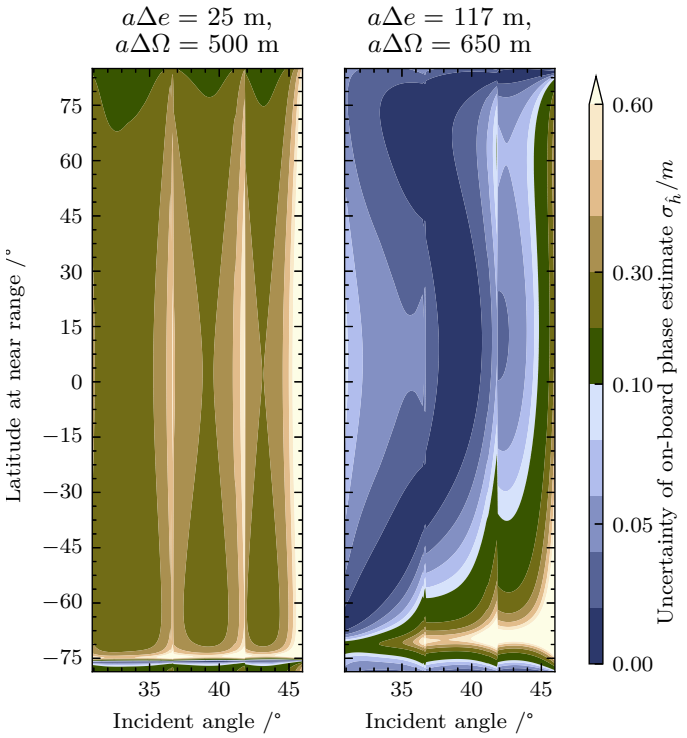


Fig. 15. The uncertainty of the phase estimate due to the along-track separation in terms of $1\sigma$ at a wind speed of $5\,\mathrm{m\,s^{-1}}$. The ATI phase estimate $\phi_{\mathrm{ATI}}$ is obtained using the two phase centers on-board each Harmony companion.

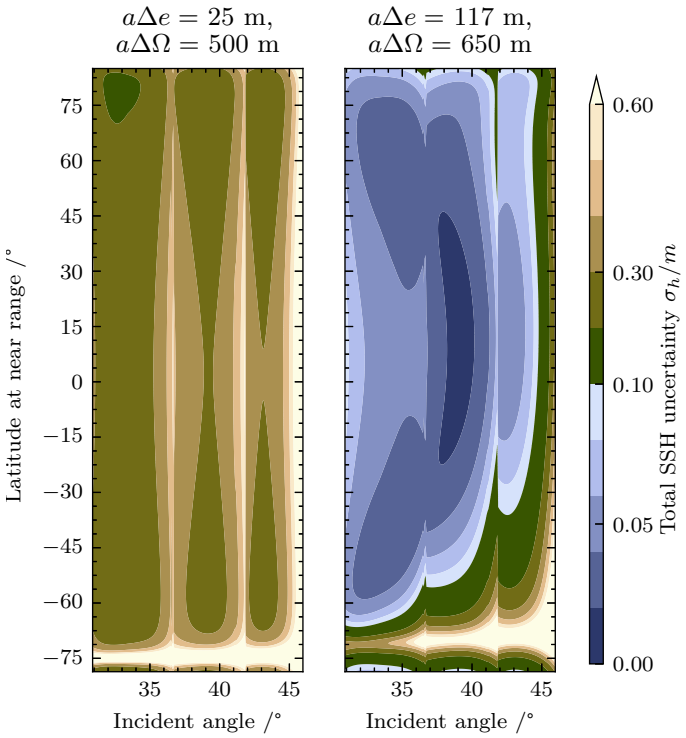


Fig. 16. The total SSH uncertainty in terms of $1\sigma$ at a wind speed of $5\,\mathrm{m\,s^{-1}}$. The total uncertainty is combined by summing the uncertainty of the interferometer shown in Figure 14 with the uncertainty due to the ATI phase estimate shown in Figure 15. In order to sum the two uncertainties the assumption that they are uncorrelated is made. From the results it can be seen that the uncertainty due to the ATI phase estimate dominates the overall performance of the interferometer.

to a maximum at the same point and compensates for the loss of along-track coherence. The orbital parameters of the second formation are chosen to minimize $B_{\parallel}$ at the midrange, resulting in a wider valley of low error in the second formation compared to the unoptimized formation. Both plots show a slight deterioration of performance at the far range due to the decrease of NRCS with increasing incidence angle.

Both plots in Figure 14 exhibit discontinuities at $\theta_i = 36.5°$ and $\theta_i = 41.9°$. The discontinuities are caused by the jumps in the NESZ of the illuminator between subswaths 1–2 and 2–3 as shown in Figure 9. These abrupt changes in the NESZ of the instrument are the result of the TOPS operation [20]. The discontinuities in the NESZ propagate to $\sigma_n$ and $\sigma_{\hat{\phi}_{\mathrm{ATI}}}$ through (20) and (16). Hence, they appear in the results of the SSH uncertainty that follow.

The second source of uncertainty comes from the ATI phase estimate produced by the two phase centers on-board the Harmony companions. The error is shown in Figure 15. Structurally the uncertainty of the ATI phase is similar to that of the system, with the error peaking close to the poles, and deteriorating towards the far-range of the swath. Yet, we observe that the error contribution of the ATI estimate is larger than the error of the system, particularly in the unoptimized formation. There are two effects driving this phenomenon:

1) The SNR of the two SAR images, coming from the individual on-board phase centers, from which the ATI phase is estimated is $4.25\,\mathrm{dB}$ worse than the SNR of the combined system. The effect of the reduced SNR is particularly visible in the mid to far range of the optimized formation.
2) The scaling factor $h_a B_{\parallel}/B_{\parallel s}$ that converts the individual estimator's standard deviation to the standard deviation of the combined system estimator increases the error. Particularly in the unoptimized formation, where $B_{\parallel}$ does not tend to $0\,\mathrm{m}$ at any point, the scaling of the error by the ratio of the system along-track baseline to the on-board baseline dominates the error.

The total error of the SSH measurement is shown in Figure 16. The total standard deviation is found using (23). The error is in the order of $10\,\mathrm{cm}$ over the majority of the swath, throughout the orbit, except towards the poles. The best performance is achieved near the Equator because at that point the formation has the largest cross-track baseline. The performance of the optimized formation shown in Figure 16 achieves a standard error of $6\,\mathrm{cm}$ or less in the near to mid range, and up to $30\,\mathrm{cm}$ in the far range. The standard error of the optimized formation at wind speeds of $10\,\mathrm{m\,s^{-1}}$ and $15\,\mathrm{m\,s^{-1}}$ is shown in Figure 17. The error is considerably improved at higher wind speeds, with $4\,\mathrm{cm}$ or less at almost the entire range and all latitudes with the exception of the

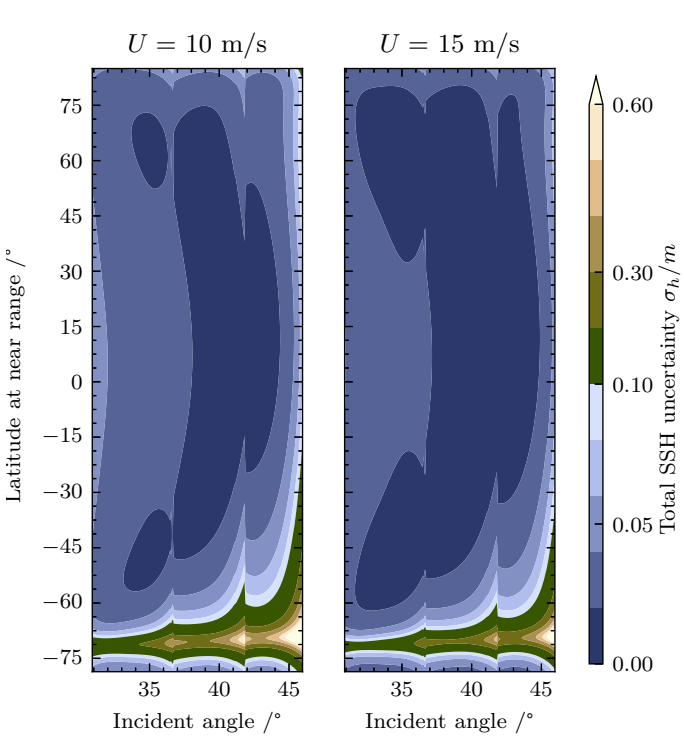


Fig. 17. The total SSH uncertainty in terms of $1\sigma$ for the optimized formation. The left panel shows the error at a wind speed of $10\,\mathrm{m\,s^{-1}}$ and the right panel at a wind speed of $15\,\mathrm{m\,s^{-1}}$.

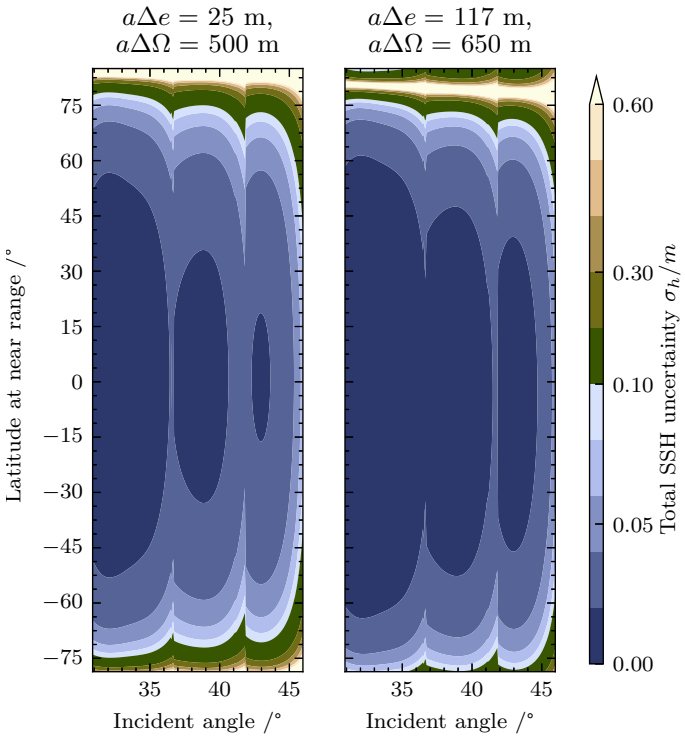


Fig. 18. The total SSH uncertainty in terms of $1\sigma$ of the quasi-monostatic interferometer at a wind speed of $5\,\mathrm{m\,s^{-1}}$.

crossing point of the Helix formation. The improvement in performance is driven by the higher SNR due to the brighter NRCS of the sea surface.

### *B. Quasi-monostatic Interferometer*

Importantly, despite the improvement that using a squinted line of sight to decrease the effective along-track baseline brings to the interferometric height estimate, there are two factors limiting the performance of a bistatic interferometer like the one presented in the Harmony case study. The first is the drop in SNR, particularly in the signal coming from the individual phase centers, at the far range which is visible at low wind speeds, where the surface is less bright. Since the SNR is driven by the NESZ of the instrument and the NRCS, improving this aspect of the performance can only be achieved by changing the design of the instrument, which is outside the scope of this paper.

The second factor is the dependence of the squint on the incidence angle. The dependence means that for a given point in the satellite formation, there is not a single squint angle that minimizes $B_{\|}$ but rather a locus of angles. Minimizing $B_{\|}$ would require a range-dependent steering of the antenna beam. For Harmony this ranges from $5°$ to $12°$, which is difficult to implement. This requirement can be relaxed if one of the satellites of the Helix formation acts as the transmitter. In other words, one of the two satellites of the Helix formation would be a monostatic SAR with the second satellite being a bistatic receiver. Overlapping the beams, while still necessary, becomes trivial and the squint is virtually range independent because the along-track transmitter-receiver separation is in the order of meters instead of kilometers.

In this section we present the performance of a quasi-monostatic SAR flying in a Helix formation with a passive companion. The antenna beams are steered according to (6) to minimize $B_{\|}$. Unless stated, parameters are kept the same with the Harmony case to highlight the effect of the squint on the performance. Figure 18 shows the standard error of the quasi-monostatic configuration.

The results show a lower error at $5\,\mathrm{m\,s^{-1}}$ compared to that of the Harmony case at the same wind speed. Sub-$5\,\mathrm{cm}$ error is achieved for the entire swath between $70°$S and $70°$N and the performance starts to degrade at latitudes higher and lower of $70°$ and $-70°$. The plots are shifted in latitude compared to those of Harmony because the main satellite of the close formation has been assumed to have the mean anomaly of S1, whereas in the Harmony case it is displaced behind S1 by $350\,\mathrm{km}$.

The degradation due to the SNR at the far range only starts to become apparent at the edge of the swath and at the two ends of the latitude where the perpendicular baseline decreases. $B_{\|}$ is kept to sub-meter values at all values of incidence angle and latitude. Thus, $\gamma_{\mathrm{ATI}}$ of the formation is kept close to 1 at the far range which keeps the total coherence is still high despite the SNR degradation. The error due to the on-board along-track phase estimate makes a negligible, sub-

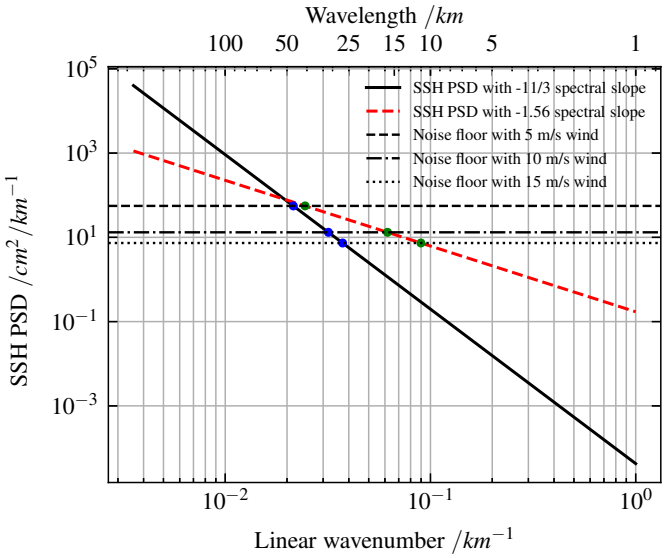


Fig. 19. The power spectral density of the sea surface height modeled using a power law and the noise floor of the Harmony interferometer. The solid black line uses a spectral slope of $-\frac{11}{3}$ which is the average at middle latitudes (30°S–60°S and 30°N–60°N). The dashed red line uses a spectral slope of $-1.56$ which is the average at low latitudes (30°S–30°N). The horizontal dashed, dashed and dotted, and dotted lines are the noise floor for wind speeds of $5\,\mathrm{m\,s^{-1}}$, $10\,\mathrm{m\,s^{-1}}$ and $15\,\mathrm{m\,s^{-1}}$ respectively. The point of intersection of the noise floor with the SSH spectrum determines the smallest wavelength that the system can resolve. The intersections of the noise floors are indicated in blue for the spectrum with $-\frac{11}{3}$ slope and green for the spectrum with a slope of $-1.56$.

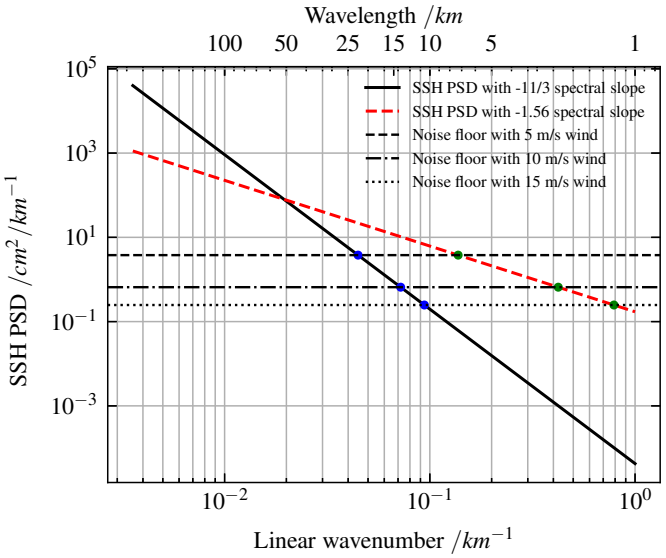


Fig. 20. The power spectral density of the sea surface height and the noise floor of the quasi-monostatic interferometer. The PSD of the SSH is the same as the one used in Figure 19.

centimeter, contribution to the total error due to the scaling factor $h_a B_{\|}/B_{\|s}$ being small.

### C. Spatial and Spectral Scales

To assess the instrument performance in terms of whether it can capture the topography of the ocean at the submesoscales (scales between $10\,\mathrm{km}$ and $100\,\mathrm{km}$), the standard deviation of the height estimate, illustrated in Figure 16, needs to be translated into a power spectral density and compared with the variation of the power spectral density of the sea surface height as a function of wavenumber. The density of the instrument's random error forms a noise floor and its intersection with the density of the SSH signal determines the spatial scales that the instrument resolves.

The power spectral density of SSH is approximated by a power law in the wavelength range of $70\,\mathrm{km}$ to $250\,\mathrm{km}$ derived from along-track altimeter observations. The spectral slope in the $30\,\mathrm{km}$ to $120\,\mathrm{km}$ wavelength range is between $-1.56$ and $-2.14$ in the low-latitude (30°S–30°N) regions [21]. The spectral slope in the $80\,\mathrm{km}$ to $280\,\mathrm{km}$ wavelength range is $-\frac{11}{3}$ in the midlatitudes (30°S–60°S and 30°N–60°N) and reaches $-5$ in the high latitude regions on average [22]. We assume that the power law that governs the SSH power spectral density extends down to $1\,\mathrm{km}$, similarly to [2], and extrapolate two SSH power spectral densities with spectral slopes of $-1.56$ and $-\frac{11}{3}$. The flatter slope is chosen for the low-latitude regions because it is derived from Sentinel-3A data which is able to resolve finer spatial scales than the altimeters which are used to derive the steeper slope [21]. $-\frac{11}{3}$ is chosen as an average slope representative of the midlatitudes. A spectral slope for high latitudes is not used in the analysis because the perpendicular baseline tends to zero in the polar part of the orbit and the interferometric performance is not representative of the system capabilities.

The instrument random error is modeled as white noise with a flat power spectral density. The spectral law for altimeter data is specified as a one-dimensional spectrum in the azimuth direction. The level of the density is determined by the variance of the error and the sampling linear wavenumber of the instrument

$$S_{hh} = \frac{\sigma_h^2}{\nu_{s_x} Q}, \tag{24}$$

where $S_{hh}$ is the power spectral density of the random error and $\nu_{s_x}$ is the sampling linear wavenumber determined by the level-2 resolution of the relative height estimate. Since the SSH density is one dimensional in azimuth, we can average the samples in range up to the Nyquist sampling interval that corresponds to the smallest scale that the interferometer should resolve. $Q$ is the oversampling factor in the range direction given by the ratio of the range sampling wavenumber to the Nyquist wavenumber.

To evaluate the noise floor against the spectral density of the measurement we set the smallest separable scale in range to $15\,\mathrm{km}$. Resolving wavelengths down to $15\,\mathrm{km}$ requires a Nyquist interval of $7.5\,\mathrm{km}$ leading to an oversampling factor of $2.5$ for a product resolution of $3\,\mathrm{km}\times 3\,\mathrm{km}$. We then convert the one-dimensional power spectral density of the error to a single-sided density by multiplying it by $2$.

We use the standard error of the relative height estimate presented in Figure 16 to compute the spectral density of the

noise floor. As previously discussed, the standard deviation of the relative height estimate varies with range and with the position of the satellite along its orbit. To compare the power spectral density of the SSH and of the error, a singular value is needed for $\sigma_h$. Because of the tendency of the error to peak towards high values at the far range that are not representative of the majority of the swath, the median of the standard deviation is used to obtain a representative average value of the standard deviation. The values at the crossing of the two companion satellites are not taken into account in the calculation because the interferometric performance at that point in the formation is not representative of the system capabilities. In the Harmony case study the median standard deviation is $4.7\,\mathrm{cm}$, $2.3\,\mathrm{cm}$ and $1.7\,\mathrm{cm}$ while in the quasi-monostatic case it is $2.0\,\mathrm{cm}$, $0.8\,\mathrm{cm}$ and $0.5\,\mathrm{cm}$ for the three wind speeds respectively. The density of the noise floor is computed by substituting the median standard error into (24). The spectral densities of the SSH, modeled with spectral slopes of $-1.56$ and $-\frac{11}{3}$, and the noise floors corresponding to Harmony and the quasi-monostatic interferometer are shown in Figures 19 and 20 respectively. We note that the error spectrum does not include systematic errors which we expect to have a non-flat spectral envelope. Thus, the resolution described in the following paragraphs shows the potential of formation-flying interferometers, rather than a complete description of the instrument resolution which will deteriorate when systematic errors with components in the submesoscale wavenumbers are included in the spectrum.

The intersection of the noise floor with the spectrum of the SSH determines the smallest wavelength that can be resolved by the instrument before the estimate is flooded by noise. The intersections of the Harmony noise floor with the steeper spectrum corresponds to wavelengths of $46.6\,\mathrm{km}$, $31.4\,\mathrm{km}$ and $26.8\,\mathrm{km}$ for wind speeds of $5\,\mathrm{m\,s^{-1}}$, $10\,\mathrm{m\,s^{-1}}$ and $15\,\mathrm{m\,s^{-1}}$ respectively. In the case of a spectrum with a flatter slope, as is the case with low-latitude regions, a more favorable performance is achieved with wavelengths of $40.8\,\mathrm{km}$, $16.2\,\mathrm{km}$ and $11.1\,\mathrm{km}$ for the same respective wave speeds. The results show that the performance is strongly dependent on wind speed. Higher wind speeds lead to a rougher ocean surface and a higher NRCS, which in turns improves the signal-to-noise ratio and lowers the noise floor. The results suggest that Harmony has the potential to resolve ocean surface height variations at spatial scales of approximately $32\,\mathrm{km}$ and $12\,\mathrm{km}$ wavelengths for moderate to high speeds.

The spectral density plot of the quasi-monostatic interferometer shows better results than the Harmony case. The noise floor intersects the steeper spectral density at wavelengths of $29.7\,\mathrm{km}$, $18.4\,\mathrm{km}$ and $14.1\,\mathrm{km}$ and the flatter density at $14.1\,\mathrm{km}$, $4.6\,\mathrm{km}$ and $2.5\,\mathrm{km}$ wavelengths. It should be noted that wavelengths below $15\,\mathrm{km}$ would not be resolvable in the range direction as a sampling interval of $7.5\,\mathrm{km}$ was assumed. The numbers represent the potential of the instrument in combination with a squinted line of sight that is optimized for a given formation. Figure 20 illustrates that the concept of using a squinted line of sight to decrease the effective along-track baseline and reduce the temporal decorrelation of the surface allows the estimation of relative SSH at submesoscales, from $30\,\mathrm{km}$ to $15\,\mathrm{km}$, at all wind conditions and over a wide swath.

TABLE III
ERROR BREAKDOWN.

| Error component | Mean value /cm | |
|---|---|---|
| | $U = 5\,\mathrm{m\,s^{-1}}$ | $U = 15\,\mathrm{m\,s^{-1}}$ |
| Instrument random error | 7.7 | 2.6 |
| Troposphere | 0.3 | 0.3 |
| Baseline | 2.2 | 2.2 |
| Phase synchronization | 1.0 | 1.0 |

### D. Error Breakdown

In addition to the random error of the instrument, systematic errors and oceanic and atmospheric biases also affect the quality of the SSH estimate. Table III contains a breakdown of the main sources of error that we expect a formation-flying interferometer that uses the optimized formation to have. Since some of the errors are strongly wind dependent, we provide mean values at wind speeds of $5\,\mathrm{m\,s^{-1}}$ and $15\,\mathrm{m\,s^{-1}}$. The random instrument error depends also on the design of the instrument and the operation of the radars (bistatic/quasi-monostatic). In Table III we show the mean instrument error of Harmony over all incidence angles and latitudes, excluding values above $45^\circ$ of incidence angle and latitudes lower than $70^\circ$S. We exclude these values because the standard error rises sharply in the last $1^\circ$ of the swath and at the latitudes when the two satellites cross, strongly biasing the mean towards a value that is not representative of the majority of the swath and latitudes.

The error due to the troposphere is assumed to be constant with wind speed and the mean value over the incidence angles is used in the table. The sea-state bias depends on the wind speed and direction. The bias will be constant over the swath and opposite in sign to near nadir looking-altimeters. We expect to achieve similar performance in terms of sea-state bias estimation and removal as near nadir-looking altimeters.

The baseline error consists of components in the along-track, perpendicular and line of sight directions. The first two are in the order of $\mathrm{mm}$, while the third has a slope in range that is significant for relative SSH estimation. We calculate the mean error in the line-of-sight direction for a resolution cell of $3\,\mathrm{km}$ by calculating the mean gradient of the error over all latitudes, except for the latitudes that the satellites cross, integrating it over the length of a resolution cell. Finally, the phase synchronization error shows an allocation of the error that a syncrhonization algorithm should achieve to ensure centimetric accuracy of the SSH estimate. The systematic errors and the oceanic and atmospheric biases are analyzed in sections IV and V respectively.

### E. Comparision With Single-platform Designs

One might wonder how a formation-flying cross-track interferometer compares to a single-platform interferometer. Recently the Surface Water and Ocean Topography (SWOT) mission has been successfully launched with the aim of providing accurate measurements of SSH at the submesoscales.

SWOT is the current state of the art single-platform ocean altimeter so it serves as a benchmark to an alternative concept such as the formation-flying XTI.

Under most conditions SWOT will achieve higher accuracy when estimating SSH. Harmony will provide similar accuracy at high, above $10\,\mathrm{m\,s^{-1}}$, wind speeds. At medium-to-high incidence angles the dominant scattering mechanism over the ocean is Bragg scattering, which increases with surface roughness. Thus, scattering and by extent accuracy increases with wind speed while nadir and side-looking swath altimeters with small incidence angles lose accuracy with wind speed because scattering is primarily specular. Furthermore, side-looking interferometers have larger swaths.

The design of Harmony had to fit in the constraints imposed by using an existing SAR satellite as an illuminator. As such, the squint of the companions is determined by the beam of the illuminator and cannot be freely optimized to reduce the effective along-track baseline throughout the swath. A quasi-monostatic interferometer would not have this constraint and achieves better performance that is comparable to SWOT. Furthermore, the benefit of a formation-flying interferometer is that the formation can be reconfigured in flight to serve the needs of different applications, such as land topography and surface current estimation.

## IV. Systematic Errors

This section provides an analysis of the systematic errors in a formation-flying interferometer. The focus is on identifying and accounting for the main bias contributions to the height estimate rather than on detailed modeling of the biases. We discuss the baseline errors and the phase synchronization error.

### A. Baseline Error

The interferometric model presented in section II-B uses the cross and along-track baselines to estimate the standard deviation of the sea surface height estimate. The model assumes knowledge of the physical separation of the formation elements, which requires knowledge of the position of the companions. Error-free position information is not possible and errors in the baseline estimation of the companions will introduce systematic errors in the height measurement.

From sections II-A3 and II-A4 we know that due to the squinted line of sight of the two SAR satellites, the along-track baseline is a function of the along-track and normal separation of the companions. The perpendicular baseline is a functions of the radial and normal components of the separation vector. As a result, an error in the normal component of the separation leads to an error in both the along-track and perpendicular baselines. A systematic error in the knowledge of the effective along-track baseline would result in a bias of the ATI phase estimate. Following (23), an error in the effective along-track baseline, $\epsilon_{\mathrm{ATI}}$, leads to a bias of the relative height estimate

$$\epsilon_h = \frac{h_a \epsilon_{\mathrm{ATI}}}{2\pi B_{\parallel}} \hat{\phi}_{\mathrm{ATI}}. \tag{25}$$

Substituting the relation between interferometric phase and radial velocity into the equation gives

$$\epsilon_h = h_a \frac{\epsilon_{\mathrm{ATI}}}{B_{\parallel}} \frac{\tau_s \sin\theta_i}{\lambda} v_r, \tag{26}$$

where $\tau_s$ is the time lag due to the on-board along-track baseline and $v_r$ is the relative radial velocity of the surface with respect to the receiver. Therefore, with a height of ambiguity of $60\,\mathrm{m}$, which is typical for the formations presented in this paper, an error in the knowledge of the effective along-track baseline of $1\,\mathrm{mm}$ translates to a height bias of $\pm 0.10\,\mathrm{mm}$ for a radial velocity of $1\,\mathrm{m\,s^{-1}}$.

Moving on to the perpendicular baseline error $\epsilon_{B_X}$. Given that the height sensitivity is inversely proportional to the perpendicular baseline, the error is [7]

$$\epsilon_h = h \frac{\epsilon_{B_X}}{B_{\perp}}, \tag{27}$$

where $h$ is the surface height. For a surface height of $h = 1\,\mathrm{m}$ and an effective perpendicular baseline of $B_{\perp} = 300\,\mathrm{m}$, a baseline error of $\epsilon_{B_X} = 1\,\mathrm{m}$ will lead to a height error of $\epsilon_h = \pm 3.3\,\mathrm{mm}$.

An error in the position of the receiver along the line of sight direction leads to an over or underestimation of the interferometric phase, resulting in a vertical displacement of the digital elevation model produced by the interferometer [7]

$$\epsilon_h = \frac{h_a}{\lambda} \epsilon_{B_l}. \tag{28}$$

As the height of ambiguity varies with look angle, $\epsilon_h$ due to an error along the line of sight changes with range. Equation (28) gives the error locally at a given range. Since the interferometric height estimate is a measure of the relative height of the surface, the slope of error is more important than the bias of the absolute value. Taking the largest value of $h_a$ for the optimized formation and dividing the difference of $h_a$ between the near and far range with the swath width gives a slope of $0.89\,\mathrm{cm}$ per kilometer of ground range for a $1\,\mathrm{mm}$ error in along the line of sight direction. This will produce a ramp in the height estimate that needs to be accounted for.

### B. Phase Synchronization Error

Bistatic radars have, by definition, separate transmitters and receivers. Each transmitter and receiver has their own modulator/demodulator and their own oscillators. The low-frequency phase errors introduced in the signal by the transmit oscillator are independent from those of the receive oscillator and do not completely cancel out when the signal is demodulated by the receiver. After demodulation the signal has a residual phase error due to the mismatch of the transmit and receive oscillator phases. The error defocuses the images produced by the SAR and produces a low-frequency modulation in azimuth in the digital elevation models. The issue applies both when two receivers operate bistatically, such as Harmony, and when one of the two instruments operate bistatically, such as the case discussed in Section III-B.

High-resolution measurement of the ocean surface topography requires synchronizing the receiver oscillators. A model

of the synchronization error is out of the paper's scope. Instead, we focus on setting the requirement of relative phase error appropriate for SSH estimation. To maintain centimetric accuracy, we set the maximum error due to the clock to $1\,\mathrm{cm}$. This translates to $0.175^\circ$ of phase error for the height of ambiguity of the optimized formation.

A potential solution is the precise orbit determination (POD)-global navigation satellite system (GNSS) scheme presented in [23]. The scheme uses a common reference oscillator for the GNSS receiver and the SAR instrument, making the residual phase error proportional to the GNSS error of the two satellites. Thus, we scale the phase error by $f_l/(\sqrt{2}f_c)$ to convert it to a synchronization error, where $f_c$ is the radar carrier frequency and $f_l$ is the carrier frequency of the navigation signal. For a radar carrier of $f_c = 5.405\,\mathrm{GHz}$ and a navigation carrier of $f_l = 1.5\,\mathrm{GHz}$ the synchronization error is $0.045^\circ$.

Alternatively, the error can be remedied in post-processing by a band-stop filter. The error affects the signal in azimuth because of the stability of the oscillator over shorter time scales. Thus, a band-stop filter with a stopband in azimuth covering the affected wavenumbers can mitigate the effect of the error at the cost of losing information over the stopband.

## V. Oceanic and Atmospheric Biases

### A. Tropospheric Path Delay

The tropospheric delay causes range geolocation errors in SAR images due to an overestimation of the distance between the instrument and the surface along the line of sight. Estimates of the troposhperic delay at the time of acquisition either from models or from radiometers can be used to correct for this range shift. The troposphere also affects interferometric height estimates of single-pass interferometers, such as the one discussed in this paper. The two SAR instruments of the interferometer image the surface with a different incidence angle. Hence, the paths from a given scatterer to each sensor undergo different tropospheric delays leading to a residual interferometric phase in the interferogram.

The shift in the interferometric phase leads to a shift in the height estimate. The error in the height estimate is proportional to the product of the tropospheric delay with the tangent of the incidence angle. The variation of the error due to the troposphere is [24]

$$\epsilon_{\mathrm{TPD}} = \left\| \delta_z(\tan^2\theta_i - 1) \right\|, \tag{29}$$

where $\delta_z$ is the nadir tropospheric path delay. The error decreases with incidence angle and reaches $0\,\mathrm{cm}$ at $45^\circ$. The dry and wet delay sum to $2.1\,\mathrm{m}$ to $2.5\,\mathrm{m}$ depending on atmospheric conditions. Without correction, this error would be too large for ocean topography estimation.

Numerical weather models, such as ERA5 from the European Center for Medium-Range Weather Forecasts (ECMWF), provide estimates of the tropospheric path delay. Using such models, we can estimate the value of $\epsilon_{\mathrm{TPD}}$ and correct for it in our estimate of the SSH. After correction, the error becomes the residual between the estimate of the nadir path delay from the model and the true value. Vieira et al. have found that the RMS error between the wet tropospheric delay and the delay measured from radiometers varies from $0.6\,\mathrm{cm}$ to $1.7\,\mathrm{cm}$ [22], depending on latitude. Taking an average value of $1.15\,\mathrm{cm}$ for the residual in the nadir direction and substituting it in (29) in place of $\delta_z$ provides an estimate of the error after correction. The error decreases from $0.6\,\mathrm{cm}$ at near range to $0\,\mathrm{cm}$ at $45^\circ$ and increases to $0.4\,\mathrm{cm}$ from $45^\circ$ to the far range. Since the $\epsilon_{\mathrm{TPD}}$ varies with incidence angle, its power spectral density will have a component in the wavenumbers that correspond to the submesoscales and the error has to be taken into account in the error budget of the interferometer.

### B. Sea-state Bias

Relative height estimates are obtained from two or more SAR images using the method of interferometry. The modulus of the interferogram is proportional to the normalized radar cross-section. The most commonly used estimator for the relative height in SAR interferometry is the maximum-likelihood estimator, which uses speckled averaged interferometric phase to estimate the relative height. The bias of an estimator is defined as the distance between the expected value of the estimator and the true value of the estimated quantity. If the NRCS is a function of height, then the expected value of the estimator will include a term proportional to the correlation of the NRCS with the height of surface which will bias the expectation away from the true value of the height.

In the case of the ocean, the waves on the surface have a difference in roughness between crests and troughs. This leads to more scattering of the SAR signal coming from the crests than the troughs [25], correlating the NRCS with the surface height. The roughness of the ocean surface depends on the wind speed and other parameters related to the state of the sea, giving the name "sea-state bias" to this phenomenon [26]. In this section we present a summary of the effect and the main findings as they related to bistatic SAR cross-track interferometers. A detailed derivation is included in the appendix.

The height estimated by an interferometer $\hat{h}(x)$ after the formation of an interferogram and averaging over independent speckle realizations is given by the convolution of the product of the NRCS $\sigma_0(x)$ and sea surface height $z(x)$ with the square of the instrument response function $\chi(x)$. For simplicity, we will consider only one dimension, so the height estimate is

$$\hat{h}(x) \approx A\frac{1}{\bar{\sigma_0}(x)}(\sigma_0 z * \|\chi\|^2)(x), \tag{30}$$

where $\bar{\sigma_0}(x) = (\sigma_0 * \|\chi\|^2)(x)$ and A is a term that includes the antenna gain and constants of proportionality. From this point on, the height estimate is computed for a region around $x_0$, and the spatial variability of the instrument-response averaged cross-section is assumed to be negligible in this region $\bar{\sigma_0}(x) = \bar{\sigma}$. Additionally, we express $\sigma(x)$ in terms of the average cross-section $\bar{\sigma}$ and a spatially varying component $\delta\sigma(x)$

$$\sigma(x) = \bar{\sigma}(1 + \delta\sigma(x)).$$

Applying this relation to (30) yields

$$\hat{h}(x) \approx A((1 + \delta\sigma)z * \|\chi\|^2)(x). \tag{31}$$

The bias of the estimator is evaluated by computing its expected value over the ensemble of the waves

$$\mathbb{E}_w[\hat{h}(x)] \approx A(\mathbb{E}_w[z(x)] + \mathbb{E}_w[\delta\sigma(x)z(x)]) * \left\|\chi(x)\right\|^2. \quad (32)$$

Equation (32) demonstrates that the estimator is biased away from the true value of the surface height $z(x)$ because of the second term that arises due to the cross-correlation of the spatial variation of the NRCS with the height. The estimator will be unbiased only in cases where the cross-correlation $\mathbb{E}[\delta\sigma(x)z(x)]$ is 0. According to the linear modulation theory of Hasselmann and Hasselmann [27], the spatial variation of the NRCS $\tilde{\delta\sigma}(k)$ is related to the surface wave amplitude $Z(k)$ via a modulation transfer function (MTF) $T(k)$ in the angular wavenumber domain

$$\tilde{\delta\sigma}(k) = T(k)Z(k). \quad (33)$$

Substituting (33) into (32) in terms of the inverse Fourier transform of $\tilde{\delta\sigma}(k)$ leads to the following expression for the bias

$$\mathrm{Bias}(\hat{h}, z) = \int T(k)\Psi(k)\,\mathrm{d}k \int \left\|\chi(x)\right\|^2 \mathrm{d}x, \quad (34)$$

where $\mathbb{E}[Z(k)Z(k')] := \Psi(k)\delta(k-k')$ is the surface elevation variance spectrum [27]. In cases where the squared instrument response function is normalized, the integral of $\left\|\chi(x)\right\|^2$ with respect to $x$ integrates to unity and the bias is determined by the integral of the modulation transfer function and the surface elevation variance spectrum.

Integrating over all numbers in $\mathbb{R}^2$ is not of interest as we only expect to come across waves with maximum wavelengths of $250\,\mathrm{m}$. Computations of (53) using the Elfouhaily spectrum [28] for $\Psi$ and the MTF defined by Schulz-Stellenfleth et al [29] for $T$ were carried out using a dimensionless fetch of $100 \times 10^3$. The bias of the height estimate due to the sea-state is shown in Figure 21 as a function of wind speed for wind azimuths of $0°$, $45°$ and $90°$, using a solid black line, a dashed red line, and a dotted blue line respectively. The bias is much stronger for winds aligned with the radar look direction than for crosswinds and increases approximately linearly with wind speed between $5\,\mathrm{m\,s^{-1}}$ to $10\,\mathrm{m\,s^{-1}}$ for all wind directions.

Quantitatively, the bias varies between $1.5\,\mathrm{cm}$ to $12.5\,\mathrm{cm}$ which is significant when compared to the standard deviation of the total random error of the height shown in Figure 16. Nevertheless, the interferometric height estimate is relative, therefore a systematic bias that is independent of ground range and azimuth will not impact the accuracy of the relative values as long as the bias does not cause the interferometric phase to wrap over $2\pi$. Given that the formations discussed have a minimum height of ambiguity of $30\,\mathrm{m}$, biases of up to $12.5\,\mathrm{cm}$ are unlikely to cause phase wrapping.

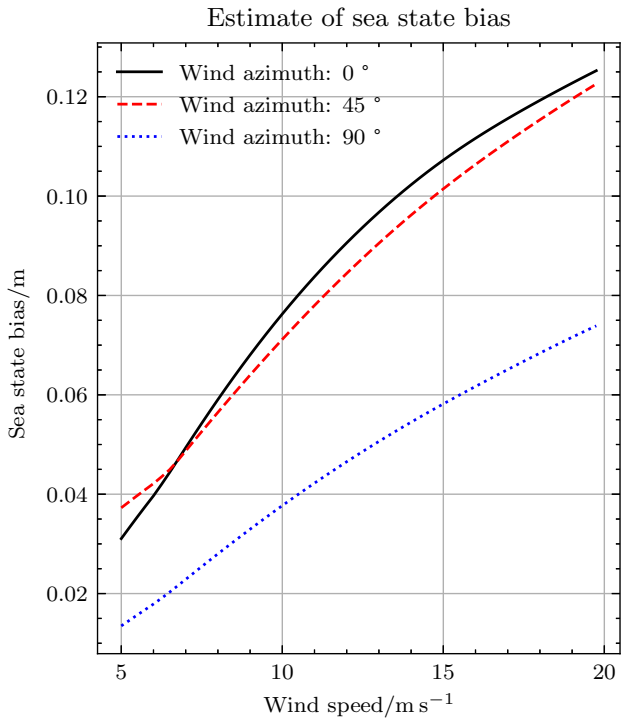


Fig. 21. Bias of the height estimate as a function of wind speed for azimuth directions of 0, 45 and 90 degrees.

## VI. Conclusion

We have presented a model to estimate the random and systematic errors in the ocean elevation measurement of a bistatic SAR interferometer with a squinted line of sight. Two case studies were used to investigate the performance of the concept: The Harmony mission in its cross-track interferometry phase; and a pair of SAR satellites flying in close formation with one acting as a transmitter and receiver and the other bistatically. The discussion has included the impact of coherence losses due to noise, volume scattering, and temporal lag between acquisitions. We investigated the simulated performance of the two systems over an orbit and the challenges involved in the estimation of relative heights from SAR images of the sea surface. The key benefit of the XTI operation of a closed formation with a squinted line of sight is allowing for effective perpendicular baselines that are sufficiently large to observe the ocean surface with sub-meter accuracy while minimizing the temporal decorrelation without compromising the safety of the formation. Minimizing the temporal delay reduces the temporal decorrelation sufficiently to allow estimation of the relative SSH.

In the case of Harmony, the squinted line of sight is a result of the bistatic operation. The beams of the companions follow that of Sentinel-1, resulting in an off-boresight line of sight at the receivers. However, bistatic operation with an illuminator that is several kilometers displaced along the orbital track is not required; the same effect can be achieved using one monostatic and one bistatic SAR system with a squinted line of sight. The performance of the interferometer can be enhanced by taking advantage of the two on-board phase centers of the receivers to estimate the contribution of the relative surface motion to the interferometric phase and remove it. The results show a standard error of $1\,\mathrm{cm}$ to $6\,\mathrm{cm}$ for the near to mid-range and up to $30\,\mathrm{cm}$ at the far range for optimized formation parameters at a wind speed of $5\,\mathrm{m\,s^{-1}}$. This corresponds to spatial scales of $47\,\mathrm{km}$ and $41\,\mathrm{km}$ for spectral slopes of $-\frac{11}{3}$ and $-1.56$ respectively. The performance improves at higher

wind speeds due to more backscattering. With a wind speed of $10\,\mathrm{m\,s^{-1}}$, wavelengths of approximately $31\,\mathrm{km}$ and $16\,\mathrm{km}$ can be resolved.

In the case of the quasi-monostatic system, the constraint to align the beam of the two SARs in the Helix formation with the beam of an illuminator that is several kilometers ahead along the track is lifted. Thus, the squint of the line of sight is not range dependent as in the case of Harmony, and can be optimized for the entire swath at all latitudes. The performance combined with the wide swath of a SAR enables the recovery of submesoscale ocean features at high wind speeds. The results of the quasi-monostatic system show a standard error of less than $5\,\mathrm{cm}$ for the entire swath with the performance degrading only near the crossing point of the formation. The error translates to resolving scales of $30\,\mathrm{km}$ for $5\,\mathrm{m\,s^{-1}}$ wind and $14\,\mathrm{km}$ for $15\,\mathrm{m\,s^{-1}}$ wind speed for the steeper spectrum.

The estimate of the sea surface height will be impacted by systematic errors. We have considered the main sources of systematic errors including phase synchronization, baseline estimation and electromagnetic modulation of the backscattered signal. The phase synchronization error has a significant impact on the estimation. Therefore, cross-track interferometers must be designed with this potential limitation in mind. Alternatively, given that the error has a known shape in the wavenumber domain, band limited in the azimuth direction and negligible in the range direction, it could be removed from the signal using a filter. A detailed derivation of the sea-state bias for both a frozen and a dynamic surface has been presented for a bistatic interferometer. In particular, we have shown that the time dependence of the backscattering does not affect the sea-state bias under the assumption of a sufficiently broad SAR processing bandwidth and that the bias is a function of the hydrodynamic modulation and the surface height variance spectrum.

In the future we would like to complete the model by providing spectral envelopes for the systematic errors and biases. Furthermore, a more complete characterization of the phase synchronization error and mitigation algorithms are needed. Finally, we would like to use the model to compute the azimuth cutoff wavenumber at different latitudes, incidence angles and wind speeds.

## Appendix
## Analysis of the Sea-state Bias

### Surface Height Estimate of a Frozen Random Backscattering Surface

In this section we investigate the sea-state bias in the height estimate produced from an interferogram for two cases: a frozen random backscattering surface, and a moving random backscattering surface. In both cases we assume that the interferogram is produced by a pair of images acquired with a zero effective along-track baseline. Consequently, the time dependence of the surface manifests itself in the scattering coefficient but not in the interferometric phase.

In the analysis, We apply the plane wave approximation to the far field of the instrument. $\boldsymbol{k_q} = k_0(\sin\psi_q, \cos\psi_q \sin\theta_q, \cos\psi_q \cos\theta_q)^T$ is the wave vector, where $\theta$ is the look angle, $\psi$ is the squint with respect to the antenna boresight, $k_0 = 2\pi/\lambda_0$ is the wavenumber of the carrier and the subscript $q \in \{T, R\}$ stands for the transmitter and the receiver respectively. $R_B$ is the bistatic range to the location where the plane wave approximation is applied. The image produced by the ith SAR of the interferometer is [30]

$$u_i(x,y) = \mathrm{e}^{-\mathrm{j}k_0 R_{B_i}} \iiint s(\boldsymbol{r'})\mathrm{e}^{-\mathrm{j}\boldsymbol{k_{B_i}}\cdot\boldsymbol{r'}}\chi(x-x', y-y')\,\mathrm{d}V', \quad (35)$$

where $s(\boldsymbol{r'})$ represents the complex scattering coefficient in a Cartesian coordinate system with the origin set at the plane wave expansion point and $x$ being the azimuth direction, $y$ the ground range direction and $z$ the elevation direction. We use the shorthand $\boldsymbol{r} = (x, y, z)^T$ for functions of $(x, y, z)$. We represent the system imaging transfer function, including the point target response and the processing filters, by $\chi(x, y)$, and the bistatic wave vector by $\boldsymbol{k_B} = \boldsymbol{k_T} + \boldsymbol{k_R}$.

Let $u_1(x, \rho)$ and $u_2(x, \rho)$ be the two SAR images forming the interferogram

$$\nu(x,\rho) = u_1(x,\rho)u_2(x,\rho)^*,$$

where the superscript $^*$ denotes complex conjugation. We assume that the scattering coefficient is a white stochastic process

$$\mathbb{E}_s[s(\boldsymbol{r_1})s^*(\boldsymbol{r_2})] = \sigma_0(\boldsymbol{r_1})\delta(\boldsymbol{r_1} - \boldsymbol{r_2}).$$

Then the expected value of the interferogram is

$$\begin{aligned} I(x,\rho) &= \mathbb{E}_s\left[\nu(x,\rho)\right] \\ &= \mathrm{e}^{-\mathrm{j}k_0\Delta R_B} \iiint\iiint \sigma_0(\boldsymbol{r'})\delta(\boldsymbol{r'} - \boldsymbol{r''}) \\ &\quad \chi(x-x', y-y') \\ &\quad \chi(x-x'', y-y'')^* \\ &\quad \mathrm{e}^{-\mathrm{j}\boldsymbol{k_{B_1}}\cdot\boldsymbol{r'}}\mathrm{e}^{\mathrm{j}\boldsymbol{k_{B_2}}\cdot\boldsymbol{r''}}\,\mathrm{d}V'\,\mathrm{d}V'', \end{aligned}$$

where $\Delta R_B = R_{B_1} - R_{B_2}$.

We use the even and sifting properties of the Dirac delta function to reduce the expected value of the interferogram to

$$I(x,\rho) = A\iiint \sigma_0(\boldsymbol{r'})\mathrm{e}^{-\mathrm{j}\Delta\boldsymbol{k_B}\cdot\boldsymbol{r'}} \left\|\chi(x-x', \rho-\rho')\right\|^2 \mathrm{d}V', \quad (36)$$

where $A = \mathrm{e}^{-\mathrm{j}k_0\Delta R_B}$ and $\Delta\boldsymbol{k}_B = \boldsymbol{k_{B_1}} - \boldsymbol{k_{B_2}}$ is the difference of the bistatic wave vectors.

We are primarily interested in the topographic mapping of the ocean surface, where we can assume that the most prominent contribution to the scattering amplitude comes from the surface. Additionally, the frozen surface $\zeta(x, y)$ is a function of the two horizontal plane coordinates describing the surface height along $z$. The slant range to a point on the surface at a given azimuth depends only on the ground range. Thus, (36) reduces to an integral over the surface

$$I(x,y) = A\iint \sigma_0(\boldsymbol{r'_p})\mathrm{e}^{-\mathrm{j}\Delta\boldsymbol{k}_{R_R}\cdot\boldsymbol{r'_p}} \left\|\chi(x-x', \rho-\rho')\right\|^2 \mathrm{d}x'\,\mathrm{d}y', \quad (37)$$

and the integral can be expressed as the convolution of the backscatter and interferometric phase terms with the norm of the system impulse response function

$$I(x,y) = A(\sigma_0\beta * \|\chi\|^2)(x,y) \tag{38}$$

where $\boldsymbol{r'_p} = (x',y')^T$ is the position vector on the surface and $\beta(\boldsymbol{r_p}) = \mathrm{e}^{-\mathrm{j}\Delta\boldsymbol{k}_{R_R}\cdot\boldsymbol{r_p}}$.

We assume that the wave height is small compared to the height of ambiguity and expand the exponential in $\beta$. The expectation of the interferogram after expanding the complex exponential is

$$I(x,y) = A(\sigma_0(1-\mathrm{j}\Delta\boldsymbol{k}_R\cdot\boldsymbol{r'_p}) * \|\chi\|^2)(x,y). \tag{39}$$

Rodriguez and Martin [31] have shown that the maximum-likelihood estimator of interferometric phase is

$$\hat{\phi} = \arctan\left(\frac{\Im\{\sum_{n=1}^{N_l}\nu[n]\}}{\Re\{\sum_{n=1}^{N_l}\nu[n]\}}\right), \tag{40}$$

where $N_l$ is the number of independent interferometric looks. Noting that for small interferometric phase $\tan\hat{\phi} \approx \hat{\phi}$, the phase and height estimators are

$$\hat{\phi} \approx \frac{\Im\{\sum_{n=1}^{N_l}\nu[n]\}}{\Re\{\sum_{n=1}^{N_l}\nu[n]\}}, \tag{41}$$

$$\hat{h} = -\frac{h_a}{2\pi}\hat{\phi}, \tag{42}$$

where $h_a$ is the height of ambiguity. Assuming that the scattering stochastic process is correlation ergodic and that we use a sufficient number of looks allows us to substitute (39) into (42)

$$\hat{h} \approx \frac{K}{\bar{\sigma}(\boldsymbol{r_p})}\iint \sigma_0(\boldsymbol{r'_p})\Delta\boldsymbol{k}_R\cdot\boldsymbol{r'_p}\left\|\chi(x-x',\rho-\rho')\right\|^2 \mathrm{d}S' \tag{43}$$

where

$$\begin{aligned}\mathrm{d}S' &= \mathrm{d}x'\,\mathrm{d}y'\\ K &= \frac{h_a}{2\pi}\\ \bar{\sigma}(\boldsymbol{r}_p) &= \iint \sigma_0(\boldsymbol{r'_p})\left\|\chi(x-x',\rho-\rho')\right\|^2 \mathrm{d}x'\,\mathrm{d}y'.\end{aligned}$$

Henceforth, we will assume that the spatial variability of the instrument-response averaged cross-section can be neglected, i.e. $\bar{\sigma}(\boldsymbol{r}_p) = \bar{\sigma}$. Additionally, we will decompose the radar cross-section into a spatially averaged constant component and a spatially varying component [32] [12]

$$\sigma_0(x,y) = \bar{\sigma} + \bar{\sigma}\delta\sigma(x,y).$$

Then (43) can be re-written as

$$\hat{h} \approx K\iint \frac{\bar{\sigma}(1+\delta\sigma(x',y'))\Delta\boldsymbol{k}_R\cdot\boldsymbol{r'_p}}{\bar{\sigma}} \left\|\chi(x-x',\rho-\rho')\right\|^2 \mathrm{d}S', \tag{44}$$

which agrees with the equation for the height measurement of the SWOT interferometer presented in [12].

We can see that the first term is proportional to the phase difference of the two SAR images, which is defined by ocean surface but the product in the second term $\delta\sigma(x',y)\Delta\boldsymbol{k}_R\cdot\boldsymbol{r'_p}$ introduces a correlation between the NRCS and the surface height that biases the estimate. The NRCS can, in the context of linear modulation theory as demonstrated by Hasselmann and Hasselmann, be expressed as a function of the surface elevation [27]

$$\sigma_0(\boldsymbol{r}_p,t) = \bar{\sigma}\left(1 + \iint_{\boldsymbol{k}} \tilde{\delta\sigma}(\boldsymbol{k})\mathrm{e}^{-j(\boldsymbol{k_w}\cdot\boldsymbol{r}_p-\omega_w t)}\,\mathrm{d}k_x\,\mathrm{d}k_\rho\right),$$

where $\boldsymbol{k}$ is the 2D wavenumber of the surface waves whose positive and negative values are included in the domain of integration. $\bar{\sigma}$ denotes the spatially averaged NRCS and $\omega_w = \sqrt{gk}$ is the gravity wave angular frequency. The cross-section modulation factor $\tilde{\delta\sigma}(\boldsymbol{k})$ and surface wave amplitude $Z(\boldsymbol{k})$ are related through the modulation transfer function (MTF) [27]

$$\tilde{\delta\sigma}(\boldsymbol{k}) = T(\boldsymbol{k})Z(\boldsymbol{k}), \tag{45}$$

where capital letters represent the Fourier transform of functions notated by the corresponding lowercase symbols. In cases where capitalization leads to a symbol which conventionally has an established meaning, e.g. $\delta\sigma$, we use the tilde to represent the Fourier transform.

Thus, the variation in cross section $\delta\sigma(x,y)$ can be expressed as the inverse Fourier transform of the product of the MTF and the surface wave amplitude

$$\frac{\delta\sigma(x,y)}{\bar{\sigma}(x_0,y_0)} = \mathcal{F}^{-1}\Big\{T(\boldsymbol{k})Z(\boldsymbol{k})\Big\}(x,y). \tag{46}$$

Equation (46) can be used to simplify (44). The dot product of the wave vector difference with the position of the resolution cell is

$$\begin{aligned}(\boldsymbol{k}_{R_1}-\boldsymbol{k}_{R_2})\cdot\boldsymbol{r} = k_{R_1}\big[&2x\sin\Delta\psi/2\cos\psi\\ &+y(\sin\theta_1\cos\psi_1 - \sin\theta_2\cos\psi_2)\\ &+z(-\cos\theta_1\cos\psi_1 + \cos\theta_2\cos\psi_2)\big],\end{aligned} \tag{47}$$

where $\psi = (\psi_{R_1}+\psi_{R_2})/2$ and we have assumed that both receivers use the same carrier frequency. In equation (47) we have made the assumption that the difference in look angles and squint is small. Substituting back to the expression for the surface wave height estimate

$$\hat{h} = Kq\left(1 + \mathcal{F}^{-1}\Big\{T(\boldsymbol{k})Z(\boldsymbol{k})\Big\}\right) z * \left\|\chi(x,\rho)\right\|^2, \tag{48}$$

with

$$q = k_{R_1}(-\cos\theta_1\cos\psi_1 + \cos\theta_2\cos\psi_2),$$

where we have expressed the MLE of the measured height as a convolution of the product of the height and cross section with the instrument response function. Additionally, we have neglected the terms proportional to $x$ and $y$ because while there is a local correlation between $(x,y)$ and the NRCS we expect that globally the offset in NRCS due to the variation of the waves in the horizontal direction will not be systematic. We express the height of ambiguity in terms of the incident and squint angles

$$\begin{aligned}h_a &:= 2\pi\left(\tfrac{\partial\phi}{\partial z}\right)^{-1}\\ &= \frac{2\pi}{k_{R_1}(-\cos\theta_1\cos\psi_1 + \cos\theta_2\cos\psi_2)}\end{aligned}$$

which simplifies the leading constant of $\hat{h}$ to unity.

To evaluate the bias of the estimator we need to compute the expected value of the estimator over the ensemble of wave surfaces. We express the expected value of the estimator in terms of the inverse Fourier transforms of $\delta\sigma$ and $z$. The focus is on the second term of (48), which we label $A(x,y) = \delta\sigma(x,y)z(x,y)$

$$\begin{aligned}\mathbb{E}_w[A(x,y)] &= \mathbb{E}_w[\mathcal{F}^{-1}\{T(\boldsymbol{k})Z(\boldsymbol{k})\}\mathcal{F}^{-1}\{Z(\boldsymbol{k})\}] \\ &= \mathbb{E}_w[\int T(\boldsymbol{k'})Z(\boldsymbol{k'})\mathrm{e}^{-j(\boldsymbol{k'}\cdot\boldsymbol{r}_p)}\,\mathrm{d}\boldsymbol{k'} \\ &\qquad \times \int Z(\boldsymbol{k''})\mathrm{e}^{-j(\boldsymbol{k''}\cdot\boldsymbol{r}_p)}\,\mathrm{d}\boldsymbol{k''}], \end{aligned} \tag{49}$$

where we can use the fact that the ocean wave field is real $z(x,y) = z(x,y)^*$ and the linearity of the expected value and the Fourier transform to simplify the expression

$$\begin{aligned}\mathbb{E}_w[A(x,y)] &= \iint T(\boldsymbol{k'})\,\mathbb{E}_w[Z(\boldsymbol{k'})Z(\boldsymbol{k''})^*] \\ &\qquad \mathrm{e}^{-j((\boldsymbol{k'}-\boldsymbol{k''})\cdot\boldsymbol{r}_p)}\,\mathrm{d}\boldsymbol{k'}\,\mathrm{d}\boldsymbol{k''} \\ &= \iint T(\boldsymbol{k'})\Psi(\boldsymbol{k'})\delta(k'_x - k''_x)\delta(k'_y - k''_y) \\ &\qquad \mathrm{e}^{-j((\boldsymbol{k'}-\boldsymbol{k''})\cdot\boldsymbol{r}_p)}\,\mathrm{d}\boldsymbol{k'}\,\mathrm{d}\boldsymbol{k''} \\ &= \int\ T(\boldsymbol{k})\Psi(\boldsymbol{k})\,\mathrm{d}\boldsymbol{k}. \end{aligned} \tag{50}$$

The definition of the surface elevation variance spectrum, as defined in [32]

$$\mathbb{E}_w[Z(\boldsymbol{k})Z(\boldsymbol{k'})] := \Psi(\boldsymbol{k})\delta(\boldsymbol{k}-\boldsymbol{k'}), \tag{51}$$

and the sifting property of the Dirac delta function were used to simplify the expression of the bias term. Substituting (50) into (48) yields

$$\begin{aligned}\mathbb{E}_w\,[\hat{h}] &= \mathbb{E}_w[z(x,y)] * \big\|\chi(x,y)\big\|^2 \\ &\quad + \int T(\boldsymbol{k})\Psi(\boldsymbol{k})\,\mathrm{d}\boldsymbol{k}\int \big\|\chi(x,y)\big\|^2\,\mathrm{d}x\,\mathrm{d}y. \end{aligned} \tag{52}$$

Equation (52) shows that the expected value of the estimator is the ensemble mean of the surface wave height filtered by the instrument response plus an additional term that is a function of the MTF and elevation spectrum. The additional term biases the estimator away from the true value of the surface height. The effect is well known in nadir altimetry as electromagnetic bias [26].

The expression for $\mathbb{E}_w\,[\hat{h}(\boldsymbol{r})]$ gives us the expected height estimate as a function of the spatial coordinates in the horizontal plane. We can obtain a measure of the bias due to the modulation of the NRCS by the surface-wave height by computing the integral of the second term in (52)

$$\mathrm{Bias}(\hat{h},z) = \iint T(\boldsymbol{k})\Psi(\boldsymbol{k})\,\mathrm{d}\boldsymbol{k}\iint \big\|\chi(x,y)\big\|^2\,\mathrm{d}x\,\mathrm{d}y. \tag{53}$$

For the purposes of investigating the effect of the instrument target response on the bias, let us assume that $\chi(x,y)^2$ is a two-dimensional squared sinc function [12]

$$\chi(x,y)^2 = \frac{1}{\delta\rho_x\delta\rho_y}\,\mathrm{sinc}\left(\frac{x}{\delta\rho_x}\right)^2\mathrm{sinc}\left(\frac{y}{\delta\rho_y}\right)^2$$

with spatial resolutions $\delta\rho_x$ and $\delta\rho_y$ in azimuth and ground range respectively. The integral over $\chi(x,y)^2$ evaluates to unity and the bias becomes a function only of the MTF and the elevation spectrum of the surface.

## Surface Height Estimate of a Moving Random Backscattering Surface

The derivation of the height bias for the case of a moving surface largely follows that of a frozen surface presented in the previous section of the appendix with a key difference. Since the surface is now not assumed to be frozen, the scattering coefficient depends on both space and time. The synthetic aperture of the instrument records the temporal variation of the scattering coefficient during the illumination time. Therefore, the interferogram and the height estimate can no longer be expressed as two-dimensional convolutions of the point target response and the NRCS as in (37) and (52).

The time dependence of the scattering coefficient means that the azimuth processing of the SAR image needs to be accounted for to arrive to an expression of the image. The derivation of the expected value of the interferometric height estimate in this section is based on Hasselmann's [32] derivation of the mean SAR image intensity for a moving surface. To make the analysis easier to follow, we only consider the azimuth coordinate of the scattering coefficient, the point target response and the impulse response of the processing filter. Given that sensing in the range direction occurs at the speed of light, we are neglecting the motion of the backscattering surface in the range dimension. The results of this subsection can be extended to the range direction by following the derivation of the previous section.

The processed signal is obtained by matched filtering in range, followed by matched filtering in azimuth. Since we are interested in the interferometric height estimate, we include in our equations the phase term due to the range to the surface that is part of the signal after range compression even though we do not go through the range processing in the analysis. Consequently, we express the processed signal as the matched filtering of the received signal and the exponential phase term

$$u_i(x) = \iint f_2(x-x'')f_1(x''-x')s(x',t'')\mathrm{e}^{-\mathrm{j}k_0R'_{B_i}}\,\mathrm{d}x'\,\mathrm{d}x'', \tag{54}$$

where $R_{B_i}$ is the bistatic range to a scatterer, $f_1(x)$ is the azimuth point target response and $f_2(x)$ is the azimuth matched filter. As noted in [32], (54) cannot be contracted into a convolution of two functions of $x$ as in (35). The azimuth point target response and the matched filter are

$$f_1(x) = \mathrm{e}^{-\mathrm{j}k_0/Rx^2}w_1(x) \tag{55}$$

$$f_2(x) = \mathrm{e}^{+\mathrm{j}k_0/Rx^2}w_2(x), \tag{56}$$

where $w_1(x)$ is the antenna pattern in azimuth and $w_2(x)$ is a weighting function over the integration time of the SAR processor $T_I$.

We substitute the transfer functions (55) and (56) in the expression for the processed signal, and after expansion of the quadratic terms in the exponentials and making a substitution for the second variable of integration, equation (54) may be

expressed as an integral over the finite resolution Fourier transform of $s(x,t)$ [32]

$$u_i(x) = \int \mathrm{e}^{-\mathrm{j}k_0 R'_{B_i}} N' \tilde{s}(x', T_I, \omega)\,\mathrm{d}x' \tag{57}$$

where

$$\tilde{s}(x', T_I, \omega) = \int w(\hat{t}, \omega) s(x', t' + \hat{t}) \mathrm{e}^{-\mathrm{j}\omega\hat{t}}\,\mathrm{d}\hat{t},$$
$$\omega = \frac{k_0 v(x - x')}{R_{B_i}},$$

and we have grouped the two filter responses into a single function

$$w(\hat{t}, \omega) = w_1(v\hat{t}) w_2\Big(\frac{R_{B_i}\omega}{k_0 v} - v\hat{t}\Big) N^{-1}.$$

The normalization factors $N$ and $N'$ are the same as in [32] with the bistatic range replacing the monostatic range.

Equation (57) is a generalized expression for the imaging of a dynamic backscattering surface analogous to that of a frozen surface (35). Therefore, we can proceed as in the previous section to obtain an expression for the height estimate using the maximum-likelihood estimator of interferometric phase. Applying the assumption that the surface is spatially white, correlation ergodic and expanding the exponential as in the case of a frozen surface yields

$$\hat{h} = \int \frac{1}{\bar{\sigma}_0(x)} N^2 \sigma_0(x', T_I) z(x') \tilde{R}_{ss}(x', T_I; \omega)\,\mathrm{d}x', \tag{58}$$

where in this case the averaged NRCS takes the form

$$\bar{\sigma}_0(x) = \int N^2 \sigma(x', T_I) \tilde{R}_{ss}(x', T_I; \omega)\,\mathrm{d}x'.$$

The model used for the expectation over the ensemble of speckle realizations is [32]

$$\mathbb{E}_s[s(x,t)s(x+x', t+\tau)] = \sigma_0(x,t) R_{ss}(x,t;\tau)\delta(x')$$

and the equivalent relation in the frequency domain is

$$\mathbb{E}_s[\tilde{s}(x, T_I; \omega)\tilde{s}(x+x', T_I; \omega)^*] = \tilde{\sigma}_0(x, T)\tilde{R}_{ss}(x, T_I; \omega)\delta(x').$$

$\tilde{R}_{ss}(x, T_I; \omega)$ is the normalized variance spectrum of the scattering element with azimuth position $x$ at a frequency offset given by $\omega$. The variance spectrum is of finite resolution due to the bandwidth of the SAR processor in azimuth which is set by the integration time $T_I$. The frequency offset $\omega$ arises due to the time dependence, i.e. the motion, of the scatterer at a given azimuth position during the integration time. The spectral components of the surface reflectivity at $x'$ are given by $\tilde{s}(x', T_I; \omega)$. The variance spectrum is a measure of the intensity of the SAR image as a function of the offset frequency. If the Doppler processing bandwidth is larger than the bandwidth of the variance spectrum then the motion of the surface results in a smearing of the height estimate without loss of spectral information.

Taking the expectation of the estimator over the wave ensemble yields

$$\mathbb{E}_w[\hat{h}] = \int \frac{1}{\bar{\sigma}_0(x)} N^2\, \mathbb{E}[\sigma_0(x', T_I) z(x')] \tilde{R}_{ss}(x', T_I; \omega)\,\mathrm{d}x'.$$

Expanding $\sigma_0(x', T_I) = \bar{\sigma}_0(x)(1 + \delta\sigma(x', T_I))$ and substituting the MTF into the expression yields an analogous expression to the one for the frozen surface but instead of the square of the imaging transfer function $\chi(x,y)^2$ we have the finite resolution variance spectrum of the scattering surface

$$\mathbb{E}_w[\hat{h}] = \int N^2\, \mathbb{E}[z(x', y)] \tilde{R}_{rr}(x', T_I; \omega)\,\mathrm{d}x' + \int T(\boldsymbol{k})\Psi(\boldsymbol{k})\,\mathrm{d}\boldsymbol{k} \int N^2 \tilde{R}_{rr}(x', T_I; \omega)\,\mathrm{d}x' \tag{59}$$

In the case of multilooking we can assume that the azimuth bandwidth of surface reflectivity is smaller than the processing bandwidth and $N^2$ is independent of frequency [32] and can be taken out of the integrals in the numerator and denominator of (58)

$$\mathbb{E}_w[\hat{h}] = \int \mathbb{E}[z(x', y)] \tilde{R}_{rr}(x', T_I; \omega)\,\mathrm{d}x' + \int T(\boldsymbol{k})\Psi(\boldsymbol{k})\,\mathrm{d}\boldsymbol{k} \int \tilde{R}_{rr}(x', T_I; \omega)\,\mathrm{d}x' \tag{60}$$

Since the variance spectrum is normalized, $\int \tilde{R}_{rr}(x', T_I; \omega)\,\mathrm{d}x'$ integrates to unity and the height bias is determined exclusively by the MTF and the elevation spectrum of the surface as in the case of the frozen surface.

## ACKNOWLEDGMENT

The authors would like to thank Prof.ir. Peter Hoogeboom for his constructive feedback during the preparation of the manuscript.

## REFERENCES

[1] G. Lapeyre and P. Klein, "Impact of the small-scale elongated filaments on the oceanic vertical pump," *Journal of Marine Research*, vol. 64, no. 6, pp. 835–851, Nov. 2006.

[2] L.-L. Fu and R. Ferrari, "Observing Oceanic Submesoscale Processes From Space," *Eos, Transactions American Geophysical Union*, vol. 89, no. 48, pp. 488–488, 2008.

[3] E. Rodriguez, B. Pollard, and J. Martin, "Wide-Swath Ocean Altimetry Using Radar Interferometry," Jul. 1999.

[4] S. D'Amico and O. Montenbruck, "Proximity Operations of Formation-Flying Spacecraft Using an Eccentricity/Inclination Vector Separation," *Journal of Guidance, Control, and Dynamics*, vol. 29, no. 3, pp. 554–563, May 2006.

[5] P. López-Dekker, H. Rott, P. Prats-Iraola, B. Chapron, K. Scipal, and E. D. Witte, "Harmony: An Earth Explorer 10 Mission Candidate to Observe Land, Ice, and Ocean Surface Dynamics," in *IGARSS 2019 - 2019 IEEE International Geoscience and Remote Sensing Symposium*, Jul. 2019, pp. 8381–8384.

[6] D. D'Aria, A. Guarnieri, and F. Rocca, "Focusing bistatic synthetic aperture radar using dip move out," *IEEE Transactions on Geoscience and Remote Sensing*, vol. 42, no. 7, pp. 1362–1376, Jul. 2004.

[7] G. Krieger, A. Moreira, H. Fiedler, I. Hajnsek, M. Werner, M. Younis, and M. Zink, "TanDEM-X: A Satellite Formation for High-Resolution SAR Interferometry," *IEEE Transactions on Geoscience and Remote Sensing*, vol. 45, no. 11, pp. 3317–3341, Nov. 2007.

[8] A. Moccia and G. Rufino, "Spaceborne along-track SAR interferometry: Performance analysis and mission scenarios," *IEEE Transactions on Aerospace and Electronic Systems*, vol. 37, no. 1, pp. 199–213, Jan. 2001.

[9] M. Seymour and I. Cumming, "Maximum likelihood estimation for SAR interferometry," in *Proceedings of IGARSS '94 - 1994 IEEE International Geoscience and Remote Sensing Symposium*, vol. 4, Aug. 1994, pp. 2272–2275 vol.4.

[10] S. Wollstadt, P. López-Dekker, F. De Zan, and M. Younis, "Design Principles and Considerations for Spaceborne ATI SAR-Based Observations of Ocean Surface Velocity Vectors," *IEEE Transactions on Geoscience and Remote Sensing*, vol. 55, no. 8, pp. 4500–4519, Aug. 2017.

[11] P. López-Dekker, Y. Li, L. Iannini, P. Prats-Iraola, and M. Rodríguez-Cassola, "On Azimuth Ambiguities Suppression for Short-Baseline Along-Track Interferometry: The Stereoid Case," in *IGARSS 2019 - 2019 IEEE International Geoscience and Remote Sensing Symposium*, Jul. 2019, pp. 110–113.

[12] E. Peral, E. Rodríguez, and D. Esteban-Fernández, "Impact of Surface Waves on SWOT's Projected Ocean Accuracy," *Remote Sensing*, vol. 7, no. 11, pp. 14 509–14 529, Nov. 2015.

[13] S. Frasier and A. Camps, "Dual-beam interferometry for ocean surface current vector mapping," *IEEE Transactions on Geoscience and Remote Sensing*, vol. 39, no. 2, pp. 401–414, Feb. 2001.

[14] F. Gatelli, A. Monti Guamieri, F. Parizzi, P. Pasquali, C. Prati, and F. Rocca, "The wavenumber shift in SAR interferometry," *IEEE Transactions on Geoscience and Remote Sensing*, vol. 32, no. 4, pp. 855–865, Jul. 1994.

[15] H. Zebker and J. Villasenor, "Decorrelation in interferometric radar echoes," *IEEE Transactions on Geoscience and Remote Sensing*, vol. 30, no. 5, pp. 950–959, Sep. 1992.

[16] E. Rodriguez and J. Martin, "Theory and design of interferometric synthetic aperture radars," *IEE Proceedings F - Radar and Signal Processing*, vol. 139, no. 2, pp. 147–159, Apr. 1992.

[17] F. Li and R. Goldstein, "Studies of multibaseline spaceborne interferometric synthetic aperture radars," *IEEE Transactions on Geoscience and Remote Sensing*, vol. 28, no. 1, pp. 88–97, Jan. 1990.

[18] Y. Yuan, "Modulation of radar observables by upper ocean dynamics," 2020.

[19] R. Torres, P. Snoeij, D. Geudtner, D. Bibby, M. Davidson, E. Attema, P. Potin, B. Rommen, N. Floury, M. Brown, I. N. Traver, P. Deghaye, B. Duesmann, B. Rosich, N. Miranda, C. Bruno, M. L'Abbate, R. Croci, A. Pietropaolo, M. Huchler, and F. Rostan, "GMES Sentinel-1 mission," *Remote Sensing of Environment*, vol. 120, pp. 9–24, May 2012.

[20] F. De Zan and A. Monti Guarnieri, "TOPSAR: Terrain Observation by Progressive Scans," *IEEE Transactions on Geoscience and Remote Sensing*, vol. 44, no. 9, pp. 2352–2360, Sep. 2006.

[21] S. Chen and B. Qiu, "Sea Surface Height Variability in the 30–120 km Wavelength Band From Altimetry Along-Track Observations," *Journal of Geophysical Research: Oceans*, vol. 126, no. 4, p. e2021JC017284, 2021.

[22] T. Vieira, M. J. Fernandes, and C. Lázaro, "Impact of the New ERA5 Reanalysis in the Computation of Radar Altimeter Wet Path Delays," *IEEE Transactions on Geoscience and Remote Sensing*, vol. 57, no. 12, pp. 9849–9857, Dec. 2019.

[23] E. Rodrigues-Silva and M. Rodriguez-Cassola, "Analysis of a POD-based Approach for Phase and Time Synchronization of Bistatic and Multistatic SAR Systems," in *EUSAR 2021; 13th European Conference on Synthetic Aperture Radar*, Mar. 2021, pp. 1–6.

[24] G. Krieger, F. De Zan, M. Bachmann, P. Lopez Dekker, M. Rodriguez Cassola, and J. S. Kim, "Tropospheric and Ionospheric Effects in Spaceborne Single-Pass SAR Interferometry and Radargrammetry," in *EUSAR 2014; 10th European Conference on Synthetic Aperture Radar*, Jun. 2014, pp. 1–4.

[25] P. Dubois and B. Chapron, "Characterization of the ocean waves signature to assess the Sea State Bias in wide-swath interferometric altimetry," in *IGARSS 2018 - 2018 IEEE International Geoscience and Remote Sensing Symposium*, Jul. 2018, pp. 3789–3792.

[26] D. Vandemark, B. Chapron, J. Sun, G. H. Crescenti, and H. C. Graber, "Ocean Wave Slope Observations Using Radar Backscatter and Laser Altimeters," *Journal of Physical Oceanography*, vol. 34, no. 12, pp. 2825–2842, Dec. 2004.

[27] K. Hasselmann and S. Hasselmann, "On the nonlinear mapping of an ocean wave spectrum into a synthetic aperture radar image spectrum and its inversion," *Journal of Geophysical Research: Oceans*, vol. 96, no. C6, pp. 10 713–10 729, 1991.

[28] T. Elfouhaily, B. Chapron, K. Katsaros, and D. Vandemark, "A unified directional spectrum for long and short wind-driven waves," *Journal of Geophysical Research: Oceans*, vol. 102, no. C7, pp. 15 781–15 796, 1997.

[29] J. Schulz-Stellenfleth, S. Lehner, and D. Hoja, "A parametric scheme for the retrieval of two-dimensional ocean wave spectra from synthetic aperture radar look cross spectra," *Journal of Geophysical Research: Oceans*, vol. 110, no. C5, 2005.

[30] R. Bamler and P. Hartl, "Synthetic aperture radar interferometry," *Inverse Problems*, vol. 14, no. 4, pp. R1–R54, Aug. 1998.

[31] E. R. Rodriguez and J. Martin, "Maximum likelihood estimation of the interferometric phase from distributed targets," *IEEE Transaction on Geoscience and Remote Sensing*, 1991.

[32] K. Hasselmann, R. K. Raney, W. J. Plant, W. Alpers, R. A. Shuchman, D. R. Lyzenga, C. L. Rufenach, and M. J. Tucker, "Theory of synthetic aperture radar ocean imaging: A MARSEN view," *Journal of Geophysical Research: Oceans*, vol. 90, no. C3, pp. 4659–4686, 1985.